1   **A multi-proxy investigation of mantle oxygen fugacity along the Reykjanes Ridge**

2

3   Davide Novella[1,*,&], John Maclennan[1], Oliver Shorttle[1,2], Julie Prytulak[3,4], and Bramley J. Murton[5]

4

5   [1] Department of Earth Sciences, University of Cambridge, UK

6   [2] Institute of Astronomy, University of Cambridge, UK

7   [3] Department of Earth Sciences, Durham University, UK

8   [4] Department of Earth Science and Engineering, Imperial College London, UK

9   [5] National Oceanography Centre, University of Southampton, UK

10

11   * corresponding author: dn345@cam.ac.uk

12   [&] now at: Department of Earth and Environmental Sciences, Università degli Studi di Pavia, Italy;

13   email: davide.novella@unipv.it

14

15

16

17

18

19

20

21

22

23

24

25

26

Abstract

Mantle oxygen fugacity (fO_2) governs the physico-chemical evolution of the Earth, however current estimates from commonly used basalt redox proxies are often in disagreement. In this study we compare three different potential basalt fO_2 proxies: Fe^{3+}/Fe_{tot}, V/Sc and V isotopes, determined on the same submarine lavas from a 700 km section of the Reykjanes Ridge, near Iceland. These samples provide a valuable test of the sensitivities of fO_2 proxies to basalt petrogenesis, as they formed at different melting conditions and from a mantle that towards Iceland exhibits increasing long-term enrichment of incompatible elements. New trace element data were determined for 63 basalts with known Fe^{3+}/Fe_{tot}. A subset of 19 lavas, covering the geographical spread of the ridge transect, was selected for vanadium isotope analyses.

Vanadium is a multi-valence element whose isotopic fractionation is theoretically susceptible to redox conditions. Yet, the $\delta^{51}V_{AA}$ composition of basaltic glasses along the Reykjanes Ridge covers only a narrow range ($\delta^{51}V_{AA}$= -1.09 to -0.86‰; 1SD= 0.02-0.09) and does not co-vary with fractionation-corrected Fe^{3+}/Fe_{tot} (0.134-0.151; 1SD= 0.005) or V/Sc (6.6-8.5; 1SD= 0.1-1.3) ratios. However, on a global scale, basaltic $\delta^{51}V_{AA}$ may be controlled by the extent of melting. The V/Sc compositions of primitive (MgO > 7.5 wt%) basalts show no systematic change along the entire length of the Reykjanes Ridge. Typical peridotite melting models in which source Fe^{3+}/Fe_{tot} is constant at 5% and that account for the increased mantle potential temperature nearer the plume center and the fO_2 dependent partitioning of V, can reproduce the V/Sc data. However, while these melting models predict that basalt Fe^{3+}/Fe_{tot} ratios should decrease with increasing mantle potential temperature towards Iceland, fractionation-corrected Fe^{3+}/Fe_{tot} of Reykjanes Ridge lavas remain nearly constant over the ridge length. This discrepancy is explained by source heterogeneity, where an oxidized mantle pyroxenite component contributes to melting with increasing proximity to Iceland.

53 Comparison of observed and modeled Fe^{3+}/Fe_{tot} indicate that source variation in fO_2 is present under

54 the Reykjanes Ridge, with higher Fe^{3+}/Fe_{tot} closer to Iceland. This source variability in fO_2 cannot

55 be resolved by V isotopes and redox-sensitive trace element ratios, which instead appear to record

56 magmatic processes.

57

58 **Keywords**

59 mantle, oxygen fugacity, MORB, Fe^{3+}/Fe_{tot}, vanadium, isotopes

60

61

62

63

64

65

66

67

68

69

70

71

72

73

74

75

76

77

78

Introduction

Oxygen fugacity is an intensive thermodynamic property that dictates the oxidizing potential of a system (e.g., Frost, 1991). In the Earth's mantle, fO_2 controls phase relations, elemental distributions and magma genesis. As magmas rise, they retain an fO_2 inherited from their source, which controls the speciation and solubility of volatile elements and thereby the composition and volume of gasses they release to Earth's atmosphere (e.g., Frost and McCammon, 2008; Gaillard et al., 2011). Knowledge of mantle fO_2 is thus fundamental for interpretation and understanding of the physico-chemical processes that control the solid-Earth's interaction with the oceans and atmosphere.

One way to determine mantle fO_2 is through the study of mantle peridotites that are either tectonically emplaced into the crust or magmatically delivered to the surface as xenoliths. Oxygen fugacity can be quantitatively estimated from such rocks by application of a mineral oxybarometer, which quantifies the thermodynamics of redox reactions between mineral phases present (e.g., olivine-orthopyroxene-spinel, O'Neill & Wall, 1987). This approach has been used to demonstrate that in the continental lithosphere, fO_2 decreases with depth, from ±2 log units relative to the FMQ (fayalite-magnetite-quartz) buffer in the spinel peridotite field to -5 ΔFMQ in the deeper garnet peridotite field (Frost and McCammon, 2008 and references therein). However, the results from these studies are primarily representative of the cratonic lithospheric mantle, from which most xenoliths derive. In contrast to the cratons, the convecting mantle is poorly sampled by xenoliths, and its distinct chemical and thermal regime means that its fO_2 may not be well described by observations of cratonic xenoliths.

Basalts are more ubiquitous samples of the convecting mantle than xenoliths. Basalts that form in equilibrium with their mantle source and subsequently remain a closed system during ascent and surface emplacement will have an eruptive fO_2 related to their mantle fO_2 (Kress and Carmichael,

105   1991). A commonly used fO_2 proxy in basalts is their ferric iron content (Fe^{3+}/Fe_{tot}), which can be

106   precisely determined by micro-scale techniques such as X-ray absorption near edge structure

107   (XANES) spectroscopy (e.g., Berry et al., 2018; Cottrell et al., 2009). Through the determination of

108   the ferric content of basalts, mantle fO_2 can be estimated following empirical thermodynamic

109   calibrations and accounting for differentiation and degassing (e.g., Brounce et al., 2014, 2017; Helz

110   et al., 2017; Kelley and Cottrell, 2012; Kress and Carmichael, 1991; Moussallam et al., 2014, 2016;

111   Shorttle et al., 2015). Previous studies (see e.g., Brounce et al., 2014, 2015, 2017; Cottrell and

112   Kelley, 2011, 2013; Hartley et al., 2017; Helz et al., 2017; Kelley and Cottrell, 2009; Moussallam et

113   al., 2014, 2016; O'Neill et al., 2018; Shorttle et al., 2015) have indicated that the upper mantle is

114   heterogeneous in terms of Fe^{3+}/Fe_{tot}, with more oxidized conditions found at arc settings ($fO_2 \geq$

115   FMQ+1) compared to mid ocean ridges (FMQ $\leq fO_2 \leq$ FMQ+0.5). Despite the prominence of using

116   Fe^{3+}/Fe_{tot} in basalts as a tool for estimating convecting mantle fO_2, some work has also returned to

117   the abyssal peridotite record to investigate its preservation of mantle fO_2. Birner et al. (2018)

118   showed that peridotites and basalts from mid-ocean ridge settings have good agreement in their

119   estimates of mantle fO_2, while new experimental work also supports this conclusion (Davis and

120   Cottrell, 2018).

121

122   Importantly, different groups' XANES-derived estimates of Fe^{3+}/Fe_{tot} in mid ocean ridge basaltic

123   glasses have recently shown offsets from each other (e.g., Berry et al., 2018; Zhang et al., 2018; see

124   Results for a discussion of our data in this context). These differences reflect underlying decisions

125   in the interpretation of the Mössbauer spectra of glasses, in particular whether at highly reducing

126   conditions the spectra record the presence of ferric iron (Berry et al., 2018). As a result, the Berry et

127   al. (2018) XANES calibration, for a given sample, estimates lower ferric iron contents than the

128   Zhang et al. (2018) calibration. Debate continues around the correct choice of calibration (Berry et

129   al., 2018; Cottrell et al., 2009; Zhang et al., 2018; see Results). However, what is more significant

130   for this study is simply the thermodynamic basis for relating ferric iron abundances to fO_2 – i.e., that

131   changes in Fe^{3+}/Fe_{tot} within a sample suite of relatively constant major element chemistry relate to

132   variation in fO_2, something which the question of XANES calibration does not directly affect.

133

134   Another potential tracer of mantle fO_2 in basalts is their V/Sc ratio, which uses the oxygen fugacity

135   dependence of the partition coefficients of V between minerals and melts $D_v^{min/melt}$ (e.g., Canil,

136   1997, 1999). Vanadium and Sc are mildly incompatible trace elements that behave similarly during

137   melting, but while Sc is homovalent in igneous systems (Sc^{3+}), V is multivalent (V^{2+}, V^{3+}, V^{4+},

138   V^{5+}). This creates an fO_2 dependence to V partitioning during melting as the different valence

139   states of V have different partition coefficients: $D_v^{min/melt}$ decreases with increasing fO_2 whereas

140      $D_{Sc}^{min/melt}$ remains constant (e.g., Canil, 1997, 1999; Mallmann & O'Neill, 2009), resulting in higher

141   V/Sc in basalts that form at more oxidizing conditions (Lee et al., 2003, 2005; Li and Lee, 2004).

142   Employing V/Sc to estimate mantle fO_2 requires a correction for fractional crystallization, and

143   therefore alternative ratios, such as V/Yb, have been proposed (Laubier et al., 2014). Importantly, in

144   contrast to Fe^{3+}/Fe_{tot}, V/Sc ratios of MORBs and arc basalts have similar values, an observation

145   which has been used to argue that the convecting mantle, whether beneath arcs or ridges, has a

146   relatively uniform fO_2 at ~FMQ-0.5 (Lee et al., 2005). Thus, current estimates of mantle fO_2

147   determined by these two commonly used proxies are in significant disagreement.

148

149   Mantle fO_2 might also be investigated by studying the stable isotopic composition of multivalent

150   transition metals in basaltic magmas (see review in Teng et al., 2017). This is because stable isotope

151   fractionation depends on valence state and coordination number. Vanadium is an element of interest

152   in this respect because of its multiple valence states. Also, V isotopic compositions are not

153   disturbed by secondary processes such as weathering or hydrothermal alteration (Prytulak et al.,

154   2013; Wu et al., 2018), which can affect other isotopic systems (e.g., Fe; Rouxel et al., 2003).

155   However, the effects of fO_2, magmatic differentiation, partial melting and source heterogeneity need

156 to be understood before applying V isotopes as a mantle fO$_2$ proxy (Prytulak et al., 2013, 2017;

157 Sossi et al., 2018; Wu et al., 2018).

158

159 In this study, a suite of mantle-derived basalts from a ~700 km long segment of the Reykjanes

160 Ridge near Iceland was selected to investigate the behaviour of Fe^{3+}/Fe$_{tot}$, V/Sc and V isotopes to

161 assess their co-variation and suitability as fO$_2$ proxies. Fe^{3+}/Fe$_{tot}$ data from Shorttle et al. (2015)

162 were recalibrated using the most recent values for the XANES reference standards (Zhang et al.,

163 2018) and combined with new trace element concentrations on 63 basalt glasses and V isotopic

164 compositions on a representative subset of 19 lavas (Fig. 1). The Reykjanes Ridge samples are well

165 characterized in terms of major and minor element concentration and display systematic variations

166 of trace element ratios and radiogenic isotopic composition with distance from Iceland (e.g., Murton

167 et al., 2002; Schilling, 1973). Pyroxenitic sources are inferred to be an important component feeding

168 magmatism on subaerial Iceland (e.g., Stapafell on the Reykjanes Peninsula where the ridge comes

169 ashore; Fig. 1), and may also extend down the ridge and affect the genesis of Reykjanes Ridge

170 basalts (Shorttle and Maclennan, 2011; Shorttle et al., 2010). In addition, the crustal thickness along

171 the Reykjanes Ridge is well determined (e.g., Jones et al., 2014 and references therein) enabling

172 precise constraints on mantle melting conditions and potential temperature (T$_p$), which gradually

173 rises by 60 °C towards Iceland (see e.g., Matthews et al., 2016). The degree of basalt differentiation

174 also increases along-ridge, as the crust thickens. Thus, the Reykjanes Ridge is an excellent locality

175 to evaluate the co-variation of potential fO$_2$ proxies during mantle melting and the influence of both

176 low-pressure differentiation and lithological heterogeneity. In addition to comparison of potential

177 proxies, thermodynamic melting models were employed to further disentangle the interplay

178 between source fO$_2$, melting, and lithological heterogeneity.

179

180 **2. Methods**

181 **2.1 Vanadium isotopes**

Chemical isolation of vanadium was conducted in the MAGIC laboratories at the Department of Earth Sciences and Engineering, Imperial College London. Clean glass shards without visible minerals, air/fluid inclusions or weathering features were hand-picked under an optical microscope and ground in an agate mortar to obtain a homogeneous, fine powder. Approximately 30 mg of each sample was weighed to provide between 5 and 10 µg of total V. The samples were digested in a 2:1 mixture of 28M HF:15 M HNO_3 at 160 °C for at least 1 day. The samples were then evaporated and re-dissolved in 15M HNO_3. This step was repeated 3-5 times in order to ensure the complete destruction of the fluorides that form during digestion. The dissolved basalts were processed through ion exchange chromatography following the protocol of Nielsen et al. (2011). This technique describes a 7-column procedure that allows for complete separation of V from the matrix and, in particular, quantitative removal of Cr and Ti that can cause isobaric interferences on the minor isotope ^{50}V.

Vanadium isotopic compositions were measured with a Nu Plasma II multi collector inductively coupled plasma mass spectrometer (MC-ICPMS) at Imperial College London following the procedure outlined in Hopkins et al. (2019). Vanadium isotopic compositions were determined by standard-sample bracketing, and are reported as permil variations relative to the Alpha Aesar (AA) V standard solution (Nielsen et al., 2011) using the standard delta notation:

$$\delta^{51}V_{AA} = 1000 \times [(^{51}V/^{50}V_{sample} / {}^{51}V/^{50}V_{AA}) - 1].$$

A secondary standard solution from BDH chemicals and the NIST 3165 solution were measured during each session to monitor instrument stability. Samples and standards were diluted to a V concentration of 600 ppb. Total procedural blanks were insignificant (< 2ng) compared to the amount of V processed. Analysis of USGS reference materials (BIR-1a, BCR-2 and AGV-2) and the BDH and NIST 3165 solution standards are in agreement with published literature (Table S1).

208

2.2 Laser ablation inductively coupled plasma mass spectrometry

Trace and rare earth element (REE) concentrations were measured by laser ablation inductively

coupled plasma mass spectrometry (LA-ICPMS) at the Department of Earth Sciences, the

University of Cambridge. This analytical setup combines a NWR193 excimer laser ablation systems

with a Perkin Elmer NexION 350D ICP mass spectrometer. The list of the trace elements analyzed

and their concentrations are reported in Table S2. Measurements were conducted on 63 polished

glasses that were previously analyzed by XANES to determine Fe^{3+}/Fe_{tot} (Shorttle et al., 2015). Spot

analyses of 100 μm diameter were conducted on clean portions of the glasses, avoiding potential

sources of contamination such as cracks or inclusions, using a laser power of 8 J/cm^2 and 10 Hz

repetition rate. These ablating conditions were optimized after testing international reference glass

standards NIST-612, BCR-2G, BIR-1G and ML3B-G and comparing with the preferred values from

the GEOREM database (available at http://georem.mpch-mainz.gwdg.de). The data were collected

by the ICP-MS using 1 sweep per reading, 50 readings and 1 replicate conditions. ICP-MS dwell

time varied for the different elements and it was typically between 10-20 ms for most trace

elements, but this value was increased up to 60 ms for some low concentrations REE. The Glitter

Software (GEMOC, Australia) was used to process raw data (signal intensity vs time), which allows

to the user to select backgrounds and signals and precisely calculate sample concentrations. The

SiO_2 content of the glasses, previously determined by electron microprobe analyses (Shorttle et al.,

2015), was used as internal standard for the normalization of trace element signals. BCR-2G was

chosen as an external standard as it provided, overall, better precision (RSD% generally <10%,

1SD) and accuracy (average percent error within ±15%) compared to other standards. These values

of precision and accuracy were calculated considering all individual analyses collected on a

particular standard at the beginning, middle and end of the session.

232

2.3 Modelling rationale

234   Two types of mantle melting scenarios were explored to reproduce the Fe^{3+}/Fe_{tot} and trace element

235   variation along the Reykjanes Ridge. The first approach was adopted to simulate adiabatic melting

236   of ambient mantle peridotite. The second was conducted to investigate the melting behavior of

237   pyroxenite and in particular the formation of enriched lavas, using the Stapafell eruption from

238   subaerial Iceland as an endmember (Fig. 1). Thermodynamic modelling was performed with the

239   pMELTS software operated through the alphaMELTS frontend (Ghiorso et al., 2002; Smith and

240   Asimow, 2005). pMELTS was used to predict the equilibrium phase assemblage of a mantle

241   composition at given conditions (P, T and fO_2). The chemical composition of the modelled

242   instantaneous melts was calculated from the phase equilibria and melting reactions. A general

243   description of the modelling rationale is provided below, while more details are reported in Table

244   S3.

245

246   *(1) DMM melting*: Depleted MORB mantle (DMM) major element composition from Workman and

247   Hart (2005) was used as a starting composition, with varying initial Fe^{3+}/Fe_{tot} ratios (4-6%)

248   calculated maintaining constant total FeO_T. These Fe^{3+} contents are chosen such that the model

249   produces melts with a range of Fe^{3+}/Fe_{tot} close to that observed. A mantle Fe^{3+}/Fe_{tot} of 4-6% is

250   slightly higher than values predicted based on mantle xenolith studies (Fe^{3+}/Fe_{tot} = 2%; e.g., Canil

251   and O'Neill, 1996). There may be two reasons for this: (1) model-based effects, whereby the

252   treatment of ferric iron in pMELTS is not accurately capturing its behavior in natural systems (e.g.,

253   the lack of ferric iron in garnet in pMELTS, despite its presence in garnet solid solution as

254   andradite); (2) the possibility that cratonic xenoliths underestimate convecting mantle fO_2 values.

255   However, this study is focused on the *relative* changes in Fe^{3+}/Fe_{tot} rather than absolute values, so

256   our choice of mantle Fe^{3+}/Fe_{tot} is less important than how it translates to basalt Fe^{3+}/Fe_{tot}, given

257   changing conditions of melt generation along ridge.

258

259   Model simulations of decompression fractional melting were conducted for changing mantle

260   potential temperatures along the Reykjanes Ridge to account for the influence of the Icelandic

261   plume on the sub-ridge thermal structure. Potential temperatures increasing from 1404 °C at ~1100

262   km to 1468 °C at ~400 km (Table S2), were constrained by matching the melt thickness produced

263   by decompression melting models of DMM with the crustal thickness reported by seismological

264   surveys (e.g., Jones et al., 2014 and references therein). Mantle fO_2 was not imposed in the models

265   and was calculated using the Fe^{3+}/Fe_{tot} ratio of the melts (Kress and Carmichael, 1991) with

266   pMELTS considering that Fe^{3+} is not incorporated in olivine and garnet. It is recognized, however,

267   that in pMELTS fO_2 can be also calculated based on solid phase equilibria (Asimow and Ghiorso,

268   1998) and that this method provides systematically less oxidized values compared with the above

269   calibration. The fO_2 determined with the Kress and Carmichael (1991) calibration was used here for

270   consistency with data from natural samples.

271

272   Adiabatic decompression models were used to calculate the major element compositions (SiO_2-

273   TiO_2-Al_2O_3-Fe_2O_3-Cr_2O_3-FeO-MgO-CaO-NaO) of progressive aggregate melts in a 2D triangular

274   melting region. Even though pMELTS allows for the direct calculation of trace element

275   concentrations, their behavior here was treated separately so that the effect of fO_2 on the distribution

276   of V between minerals and melts could be incorporated (e.g., Canil, 1997). Partition coefficients of

277   V were calculated following the parameterization of Mallmann and O'Neill (2009, 2013) while

278   those for selected trace elements (Sc, Ba, La, Nb, Zr, K) used the values of McKenzie & O'Nions

279   (1991, 1995) and Mallmann & O'Neill (2009). These particular elements were chosen to monitor

280   the behavior of trace element ratios in the models and track enrichment along the ridge (see

281   discussion). The trace element compositions of the melts were calculated assuming a depleted

282   mantle source of Salters & Stracke (2004), which provide concentrations for all elements of interest,

283   and the phase compositions, modal abundances and P, T and fO_2 from the pMELTS calculations.

284

285 *(2) Pyroxenite melting*: Modelling the composition of melts produced by melting of a bi-lithological

286 mantle, containing a mechanical mixture of peridotite and pyroxenite, is challenging due to the

287 variety of melt-rock reactions that can occur. pMELTS does not currently allow for direct

288 calculation of melting of a bi-lithological mantle and instead a multi-step approach, where the

289 lithologies are modelled separately and combined, needs to be followed (Rudge et al., 2013). A

290 further complexity for modelling pyroxenite melting is that its low solidus temperature means that

291 melting begins above 4 GPa at the potential temperatures investigated here, which is outside the

292 calibrated pressure range of pMELTS. We therefore made a first-order investigation of pyroxenite's

293 effect on the composition of aggregate melts, discounting the full chemical and physical complexity

294 a more complete model would need to incorporate. Only an initial stage of isobaric melting of

295 mantle pyroxenite was modelled here, as described by Rudge et al. (2013). This approximates

296 adiabatic decompression melting by instead conducting isobaric melting calculations in the

297 calibrated pressure range of pMELTS. Assuming that the melt productivity (i.e., dF/dP) is known

298 for the pyroxenite, the isobaric calculations can be approximately related to a decompression

299 interval. Low-degree model melts are finally compared to Stapafell lavas in order to assess trace

300 element enrichment of Reykjanes Ridge basalts.

301

302 The pyroxenite chosen for modelling was KG1 from Kogiso et al. (1998), which compositionally

303 corresponds to a 1:1 peridotite:basalt mixture. The Fe^{3+}/Fe_{tot} of this lithology was set at 16%

304 assuming KG1 represents a peridotite with 5% Fe^{3+}/Fe_{tot} (DMM models) mixed with a Proterozoic

305 basalt with 27% Fe^{3+}/Fe_{tot} ratio (e.g., Stolper and Keller, 2018). Proterozoic basalts can be

306 envisaged as remnant subducted slab in the mantle that were oxidized during seafloor weathering

307 (Stolper and Keller, 2018). The trace element concentrations of KG1 were also calculated by

308 mixing peridotite from Salters and Stracke (2004) with recycled oceanic crust from Stracke et al.

309 (2003). If not reported in Stracke et al. (2003), the concentration of certain elements of the recycled

310 oceanic crust were calculated using the N-MORB mean of Gale et al. (2013) and the

12

311 supercomposite altered MORB composition from Bach et al. (2003). Concentrations of elements

312 with high mobility were recalculated using the dehydration model of Stracke et al. (2003). Model

313 calculations were performed for a pressure of 3 GPa, which corresponds to the onset of melt

314 extraction of DMM source at the highest T_p (approaching Iceland). Partition coefficients varying

315 with P, T and composition were used and no fixed fO$_2$ was imposed (Table S3).

316

317 **3. Results**

318 **3.1 Vanadium isotopic compositions**

319 The V isotopic composition of the Reykjanes Ridge basalts ranges between -1.09 and -0.86‰

320 (Table S2), and extends towards lighter values from the global average for MORB (-0.84‰ ± 0.10

321 2SD, n= 22; Wu et al., 2018). No systematic variation is observed along the 700 km transect of the

322 ridge (Fig. 2), with Fe^{3+}/Fe_{tot} (Fig. 3a) or with V/Sc ratio (Fig. 3b). The average of all Reykjanes

323 Ridge basalts is -0.97‰ ±0.17 2SD (n=19) and overlaps with the MORB average value of Wu et al.

324 (2018). In detail, the Reykjanes Ridge basalts are the light isotope end-member in the positive

325 global correlation between Na_8 and $\delta^{51}V$ determined by Wu et al. (2018) (Fig. 4).

326

327 **3.2 Trace elements**

328 Trace element concentrations are summarized in Table S2. The V/Sc ratios range between 6.5 and

329 10 and are displayed in Fig. 5 as a function of distance from Iceland and MgO content. The V/Sc

330 ratio increases approaching Iceland, however, this signal negatively correlates with MgO contents

331 indicating the strong effect of fractional crystallization (e.g., Li and Lee, 2004). Specifically, Fig. 6

332 shows that samples with V/Sc > 8.5 have CaO <11.9 wt% and MgO <7.3 wt%, demonstrating that

333 low pressure clinopyroxene fractionation is responsible for fractionating V from Sc (Fig. S1).

334 Primitive Reykjanes Ridge basalts with MgO >7.5 wt%, however, are not affected by

335 clinopyroxene crystallization (Fig. 6 and S1) and show no systematic changes in V/Sc along the

336   ridge ranging between 6.5 and 8.5, in agreement with the average MORB value of 6.7 (Lee et al.,

337   2005).

338

339   The incompatible trace element ratio Nb/Zr increases from 0.02 at 1100 km to 0.11 at 400 km

340   distance along the Reykjanes Ridge (Table S2), which has been interpreted to reflect a greater

341   proportion of plume-fed enriched material closer to Iceland (e.g., Murton et al., 2002; Schilling,

342   1973; Shorttle and Maclennan, 2011). Short length scale heterogeneity along the Reykjanes Ridge

343   is also shown by the chemically anomalous seamount 14D, which has Nb/Zr =0.08 at ~1100 km

344   from the Icelandic plume center (Table S2). This is 4 times above local background values and

345   closer to the average crustal composition of subaerial Iceland (Shorttle et al., 2015).

346

347   **3.3 Fe^{3+}/Fe_{tot} ratios revisited from Shorttle et al. (2015)**

348   Shorttle et al. (2015) performed micro XANES on the same Reykjanes Ridge basalts that were

349   investigated in this study. Their work determined their Fe^{3+}/Fe_{tot} ratios using the standards from the

350   Smithsonian NMNH (catalog #117393) described in Cottrell et al. (2009). By evaluating time-

351   resolved XANES spectra, Shorttle et al. (2015) ruled out beam damage causing oxidation effects.

352

353   However, since the work of Shorttle et al. (2015), cryogenic Mössbauer analyses were used to re-

354   determine the Fe^{3+}/Fe_{tot} ratios of the standards developed by Cottrell et al. (2009), with the original

355   Mössbauer work having been performed at room temperature (Zhang et al., 2018). Zhang et al.'s

356   (2018) re-analysis of the standards provides lower Fe^{3+}/Fe_{tot} estimates, with their work suggesting a

357   differential temperature-dependent response of the Fe^{3+} and Fe^{2+} Mössbauer doublets that has

358   compromised previous room-temperature Mössbauer work. As such, when the raw XANES spectra

359   of Shorttle et al. (2015) were reprocessed in this study using the Zhang et al. (2018) calibration,

360   their Fe^{3+}/Fe_{tot} decreased (Table S2). Additionally, a more conservative measure of how to relate

361   spectral shape to Fe^{3+}/Fe_{tot} was used in the quantifying of the XANES spectra here than had

362   originally been used by Shorttle et al. (2015) (who employed a principal component regression of

363   the entire pre-edge region). The peak area ratio was used in this study to form a calibration

364   following Zhang et al. (2016), as it showed the least compositional sensitivity. Although there is

365   limited major element variability in this sample suite, what variation there is co-varies with distance

366   along ridge (via igneous differentiation), so the peak area ratio approach minimizes that chance that

367   this is aliased into Fe^{3+}/Fe_{tot} estimates.

368

369   Berry et al. (2018) and O'Neill et al. (2018) have recently argued for a different interpretation of the

370   Mössbauer spectra underpinning the Fe^{3+}/Fe_{tot} of the XANES standards of Cottrell et al. (2009).

371   This interpretation would suggest that the recalibrated Shorttle et al. (2015) Fe^{3+}/Fe_{tot} should be

372   systematically lowered by a further 2-3% (absolute). However, the differences between the Berry et

373   al. (2018) and the Zhang et al. (2018) calibrations do not translate to significant differences in

374   inferred fO_2, because the Berry et al. (2018) calibration has been linked to a re-parameterization of

375   how basalt Fe^{3+}/Fe_{tot} is related to fO_2 (O'Neill et al., 2018). The result is that either using Zhang et

376   al. (2018) with Kress and Carmichael (1991), or Berry et al. (2018) with O'Neill et al. (2018), the

377   inferred mantle fO_2 from basalts is nearly constant at ~FMQ.

378

379   Importantly, it is emphasized that this study is focused on understanding *relative* fO_2 variation along

380   the Reykjanes Ridge and how this is reflected in changes in the various fO_2 proxies. As such,

381   further comments on the cause of absolute discrepancies in Mössbauer-based XANES calibrations

382   are not developed.

383

384   The recalibrated Fe^{3+}/Fe_{tot} data of the Reykjanes Ridge basalts are reported in Table S2 and

385   displayed in Fig. 7a. The raw Fe^{3+}/Fe_{tot} ratios range between 0.141 and 0.162, which is lower than

386   the range of 0.155 to 0.175 previously reported by Shorttle et al. (2015). The highest values are

387   observed in the seamount samples 17D1 (0.158) and 14D (0.162) that are recognized as local

388   heterogeneities (Murton et al., 2002; Shorttle et al., 2015), with the rest of the Reykjanes Ridge

389   basalts reaching a maximum Fe^{3+}/Fe_{tot} ratio of 0.157. An error on Fe^{3+}/Fe_{tot} of 0.5% (absolute) is

390   estimated from the long term reproducibility of the standards used during the XANES sessions of

391   Shorttle et al. (2015).

392

393   The effect of crystallization on the ferric iron content of the lavas (e.g., Cottrell and Kelley, 2011)

394   can be seen in Fig. 7a, where more evolved basalts with lower MgO have higher Fe^{3+}/Fe_{tot} ratios.

395   The raw data calculated here were corrected for crystallization using the two-stage approach of

396   Shorttle et al. (2015), which combines a an empirical correction to 8 wt% MgO with olivine

397   addition to 10 wt% MgO. Results are shown in Fig. 7b, where Fe^{3+}/Fe_{tot} ratios corrected to 10 wt%

398   MgO (MgO_{10}) are now shifted to lower values between 0.131 and 0.151. These Fe^{3+}/Fe_{tot} ratios are

399   in agreement with recent MORB averages (0.143) determined by Zhang et al. (2018) using

400   XANES. The fractionation-corrected Fe^{3+}/Fe_{tot} (Fig. 7b) are used in the discussion that follows and

401   for comparison with model results. Oxygen fugacities calculated using the Fe^{3+}/Fe_{tot} MgO_{10} ratios

402   and the calibration of Kress and Carmichael (1991) at 2 kbar range between QFM+0.06 to QFM-

403   0.32 (Fig. 7c). However, it is remarked again that rather than absolute Fe^{3+}/Fe_{tot} ratios, this study

404   focuses on the differences between natural and modelled observations.

405

406   **3.4 Melting models**

407   Given the restricted range of $\delta^{51}V$, the lack of systematic co-variation with other chemical

408   parameters (Fig. 2, 3) and the scarcity of isotopic mineral-melt fractionation factors, modelling

409   focused on reproducing the Fe^{3+}/Fe_{tot}, V/Sc and Nb/Zr ratio of the melts along the Reykjanes Ridge

410   (Fig. 8, Table S4).

411

412   In all DMM melting models, garnet is the first phase to disappear from the mantle residue during

413   decompression melting, followed by clinopyroxene. For example, for the DMM composition with

414 5% bulk Fe^{3+}/Fe_{tot} and at the lowest T_p investigated (1404 °C), garnet disappears at approximately

415 2.2 GPa and clinopyroxene at 0.8 GPa. The same behavior is observed at higher T_p, with phases

416 being consumed in the solid assemblage at slightly higher pressures. At T_p = 1404 °C, melt is first

417 produced at approximately 1.9 GPa and is first extracted from the peridotite at slightly shallower

418 depths, 1.8 GPa, when minimum porosity values of 0.5% (vol.) are reached (see constrains from

419 e.g., Sims et al., 1999). At the highest T_p investigated (1468 °C), melts begin to form at higher

420 pressure, 3.4 GPa, and begin separating from the residue at 3.0 GPa. Aggregate melt calculations

421 stop at the base of the crust (determined by pressure of the overlying melt-derived crust) at a

422 particular T_p along the Reykjanes Ridge. These pressures at the base of the crust range from 0.21

423 GPa in the south to 0.32 GPa at the northern most section of the ridge, corresponding to crustal

424 thicknesses of ~7 and 11 km, respectively (assuming 2900 kg/m^3 as an average crustal density).

425 Over the 1404 °C to 1468 °C T_p range considered, maximum extents of melting (F) increase from

426 25% to 29%.

427

428 Modelled Fe^{3+}/Fe_{tot} ratios of the aggregate melts decrease towards Iceland as higher potential

429 temperatures are encountered (Fig. 8a; Table S4). Depending on source Fe^{3+}/Fe_{tot}, decreases of

430 between 0.02 and 0.03 Fe^{3+}/Fe_{tot} in the modelled aggregate melt compositions are observed as T_p

431 increases by 64 °C (i.e., from 1404 °C to 1468 °C), with associated decrease in melt absolute fO_2

432 between 0.78 and 0.83. This result is consistent with the findings of Gaetani (2016), who also

433 showed that higher mantle temperatures produce more reduced aggregate melts. The calculated

434 V/Sc ratio of partial melts produced also reflects changes in fO_2 (Fig. 8b), indicating an increased

435 average D_V/D_{Sc} during melting towards Iceland (Table S4). However, V/Sc only exhibits a low

436 amplitude response to these changing melting conditions, varying by only 0.7-0.9 at a given

437 Fe^{3+}/Fe_{tot} source concentration over the investigated range of T_p (Fig. 8b). As expected for highly

438 incompatible and fO_2 insensitive elements, the calculated Nb/Zr ratio in the melts are near constant

439 at ~0.03 along the Reykjanes Ridge (Fig. 8c), regardless of the initial bulk Fe^{3+}/Fe_{tot} (Table S4).

440

The pyroxenite modelling focused on calculating Fe^{3+}/Fe_{tot} and trace element ratios, where

disparities between the melt concentrations from the DMM models and the Reykjanes Ridge basalts

are observed at distances < 700 km to Iceland (Fig. 8a, c). The low-degree (F%= 0.2 to ~20%) melt

compositions formed in the KG1 pyroxenite melting models are reported in Table S5. In the

isobaric melting model at 3 GPa, pyroxenite starts melting at 1384 °C and melts are extracted from

the solid assemblage (consisting of olivine + garnet + clinopyroxene + spinel) at 1394 °C, when the

porosity is higher than 0.5% (vol.). With increasing temperature, orthopyroxene becomes a stable

phase in the solid assemblage with abundances increasing as melting proceeds. This is contrary to

clinopyroxene abundances, which decrease as it is consumed on melting. Spinel is the least

abundant phase in the solid assemblage and its abundance also slightly decreases with increasing

temperature. As a result of these melting reactions, the liquid's Fe^{3+}/Fe_{tot} increases with increasing

extent of melting as clinopyroxene (the dominant phase in the solid assemblage and major host of

Fe^{3+}) and spinel (another reservoir of Fe^{3+} in its magnetite component) are progressively consumed.

Trace element ratios used to indicate enrichment towards Iceland (e.g., Nb/Zr, La/Yb) are high in

these melts (Table S5). For example, the calculated Nb/Zr ratio of the isobaric melts produced by

melting KG1 pyroxenite ranges between 0.12 and 0.04 at melt fractions 0.2 and 20%, respectively,

which are higher than the ratios produced in the DMM models at any T_p (Table S4).

458

Discussion

4.1 Vanadium isotopes as an fO_2 proxy

The $\delta^{51}V$ measured thus far in basaltic lavas with >4 wt% MgO have limited variation (Prytulak et

al., 2013, 2017; Wu et al., 2018). However, an increase of ~2‰ in $\delta^{51}V$ towards heavier $\delta^{51}V$ values

during progressive closed-system fractional crystallization of genetically related magmas has been

ascribed mainly to the crystallization of isotopically light iron oxides (Prytulak et al., 2017; Sossi et

al., 2018). The Reykjanes Ridge basalts investigated in this study all have MgO contents >6.3 wt%

466 (Shorttle et al., 2015), and thus fractional crystallization is not expected to influence their V isotopic

467 signatures. The Reykjanes Ridge basalts display coherent and significant variation in trace element

468 (e.g. Nb/Zr) and radiogenic isotopic compositions (e.g., $^{87}Sr/^{86}Sr$ and $^{143}Nd/^{144}Nd$; Murton et al.,

469 2002). Increasing enrichment along the Reykjanes Ridge on approach to Iceland is commonly

470 interpreted as the influence of the Icelandic mantle plume (e.g., Murton et al., 2002; Schilling,

471 1973). Murton et al. (2002) explained the geochemical variations of the Reykjanes Ridge basalts by

472 mixing of six differently enriched mantle components. Thus, the data presented here suggest that V

473 isotopes are not sensitive to the chemical heterogeneities in the mantle source below the Reykjanes

474 Ridge documented by trace element and radiogenic isotope systems. This point is emphasized by

475 the unremarkable V isotopic composition of sample 14D of $\delta^{51}V$ = -1.09 (Fig. 2), which in terms of

476 its trace elements and radiogenic isotopes clearly samples a local mantle compositional

477 heterogeneity.

478

479 Wu et al. (2018) recently proposed that V isotope fractionation may be sensitive to the extent of

480 melting by demonstrating a positive correlation between $\delta^{51}V$ and Na_8, an indicator of the degree of

481 melting (Klein and Langmuir, 1987). The Reykjanes Ridge basalts have Na_8 between 1.83 and 2.19,

482 and are displaced to isotopically lighter values compared with higher Na_8 MORB (Fig. 4). The

483 Reykjanes Ridge basalts follow the general trend established by Wu et al. (2018), supporting the

484 notion that the extent of melting may influence the V isotopic composition of MORBs on a global

485 scale.

486

487 Importantly, the V isotopic compositions of the Reykjanes Ridge basalts do not correlate with

488 Fe^{3+}/Fe_{tot} or V/Sc (Fig. 3). This observation indicates that V isotopes of primitive basalts are not

489 sensitive to an fO_2 difference of ~0.3 log unit along the Reykjanes Ridge. However, primitive

490 samples not affected by fractional crystallization and equilibrated at more extreme fO_2 conditions,

491   need to be analyzed to further assess the sensitivity of V isotopes to redox conditions for their use as

492   an fO$_2$ sensor.

493

494   **4.2 V/Sc as an fO$_2$ proxy**

495   The V/Sc ratio of the partial melts calculated by pMELTS are compared to the Reykjanes Ridge

496   compositions in Fig. 8b. The $D^{peridotite/melt}$ of trace elements is calculated based on $D^{min/melt}$ and the

497   modal abundances of the minerals in the solid residue, which change as a function of T_p and P

498   during decompression. The average V partition coefficients increase towards Iceland, where higher

499   potential temperatures are met and resultingly lower fO$_2$'s are calculated; the average Sc partition

500   coefficient only slightly increases towards Iceland due to the deeper onset of melting, meaning that

501   garnet is residual in the phase assemblage during proportionally more of the melting interval, and

502   garnet has the highest D_{Sc} (Table S4). The net effect of these processes is for D_V/D_{Sc} to increase

503   towards Iceland, resulting in the gently decreasing V/Sc ratio observed in the accumulated partial

504   melts generated by pMELTS (Fig. 8b). The melting model of DMM with initial 5% Fe^{3+}/Fe_{tot}

505   reproduces, within error, the V/Sc ratios of the primitive (>7.5 wt% MgO) Reykjanes Ridge basalts

506   along the entire extent of the ridge between 1100 and 400 km (Fig. 8b). The V/Sc of primitive

507   basalts translates into fO$_2$'s ranging between ΔFMQ = 0 to -0.5 following the model of Lee et al.

508   (2005). These fO$_2$ values are consistent with those calculated from the Fe^{3+}/Fe_{tot} (Fig. 7c). However,

509   interpretations of mantle fO$_2$ values determined by V/Sc proxy are model-dependent, as the V/Sc

510   concentration of basalts depends on both $D_v^{min/melt}$ and $D_{Sc}^{min/melt}$, the source concentrations and the

511   fO$_2$ conditions. For example, Prytulak et al. (2017) used batch melting calculations to illustrate that

512   a less oxidized, fertile mantle and a more oxidized, depleted mantle, with respectively higher and

513   lower $D_v^{pdt/melt}$, can produce similar V/Sc ratios in MORB and arc lavas, highlighting the limitations

514   of V/Sc as a direct redox proxy (see also Bucholz and Kelemen (2019) for this discussion in an arc

515   context).

516

4.3 Fe^{3+}/Fe_{tot} as an fO_2 proxy

The ferric iron content of partial melts formed during adiabatic decompression of mantle peridotite reflects both source Fe^{3+}/Fe_{tot} and T_p. At a fixed source Fe^{3+}/Fe_{tot}, the upwelling mantle peridotite crosses fO_2 isopleths that become slightly more oxidized through the spinel stability field (Gaetani, 2016). Instantaneous melts may therefore become more oxidized as decompression proceeds. However, aggregate melts are also sensitive to the onset of melting, and when melting begins in the garnet field, at $Tp > 1447$ °C, the Fe^{3+}/Fe_{tot} of the aggregate melts decreases until garnet is exhausted from the solid assemblage. The net effect is that the Fe^{3+}/Fe_{tot} of aggregate melts decreases with increasing potential temperatures (Gaetani, 2016), as observed in the model runs as Iceland is approached (Fig. 8a).

Melting models of DMM composition with 5% initial Fe^{3+}/Fe_{tot} reproduce the Reykjanes Ridge basalt compositions between ~700 and 1100 km from the plume, in agreement with the V/Sc data (Fig. 8a-b). The highest Fe^{3+}/Fe_{tot} ratios of seamounts 14D and 17D, which formed from particularly enriched sources far from Iceland (Murton et al., 2002), are in agreement with the model, given the 0.01 2SD uncertainty of XANES analyses of Fe^{3+}/Fe_{tot}. Notably, within ~700 km of the Icelandic plume, the Fe^{3+}/Fe_{tot} ratio of natural samples clearly deviate from that of modelled partial melts. While Fe^{3+}/Fe_{tot} ratio in modelled partial melts decreases monotonically by 0.02-0.03 towards Iceland, the Reykjanes Ridge basalts remain nearly constant (Fig. 7a-b). The Fe^{3+}/Fe_{tot} ratio of the Reykjanes Ridge basalts at 400 km distance can be reproduced by melting DMM with a higher initial Fe^{3+}/Fe_{tot} content (6%, Fig. 8a). However, deviations from the models in both Fe^{3+}/Fe_{tot} and trace element ratios at approximately 700 km from Iceland require the mantle source heterogeneity, as is documented by radiogenic isotopes (e.g., Murton et al., 2002). For example, a difference of 0.02 Fe^{3+}/Fe_{tot} between natural and modelled melts is reached at 400 km distance (Fig. 8a), which is twice the conservative uncertainty of the XANES analyses (0.01 2SD). Shorttle et al. (2015) suggested that the presence of recycled, oxidized oceanic crust in the mantle sampled by the

543   Icelandic plume may explain the trace element and Fe^{3+}/Fe_{tot} signatures. The Fe^{3+}/Fe_{tot} ratios of the

544   Reykjanes Ridge basalts are therefore sensitive to the melting conditions and, importantly, to the

545   presence of chemical heterogeneities in the mantle source as observed in the northern part of the

546   ridge segment (Fig. 8a). The higher Fe^{3+}/Fe_{tot} signal observed in the Reykjanes Ridge basalts near

547   Iceland, compared to modelled concentrations of DMM with 5% Fe^{3+}/Fe_{tot}, can be explained by the

548   presence of pyroxenite in the source. Calculated partial melts of KG1 pyroxenite have high

549   Fe^{3+}/Fe_{tot} (up to 0.187, Table S5), which if mixed with melts produced from a nominal DMM

550   peridotite will counterbalance the Fe^{3+}/Fe_{tot} decrease predicted from T_p effects alone. Notably, the

551   more oxidized signature towards Iceland recognized by the Fe^{3+}/Fe_{tot} difference between the

552   Reykjanes Ridge basalts and the DMM model prediction is not recorded in the V/Sc ratios (Fig.

553   8b).

554

555   **4.4 The influence of a more oxidized and enriched source on the geochemistry of Reykjanes**

556   **Ridge basalts near Iceland**

557   The Nb/Zr concentrations of partial melts produced by DMM melting models (~0.03) are similar to

558   the Reykjanes Ridge basalts between 1100-700 km (Fig. 8c). However, Nb/Zr deviates from model

559   predictions at approximately 700 km and a ten-fold difference between the Reykjanes Ridge basalts

560   and the partial melts produced by DMM models is reached at 400 km (Fig. 8c). The deviation of

561   Nb/Zr ratios between the RR basalts and DMM models coincides with Fe^{3+}/Fe_{tot} mismatches (Fig.

562   S2), indicating the combined oxidized and enriched nature of the mantle source sampled by the

563   Reykjanes Ridge basalt close to Iceland.

564

565   In order to investigate the effect of lithological heterogeneity on Fe^{3+}/Fe_{tot} and trace elements used

566   as an indicator of enrichment, lavas from Stapafell were considered as a proxy for enriched melts.

567   Stapafell is one of the most enriched basalts on the Icelandic rift zone (Fig. 1) with high trace

568   element ratios (e.g., Nb/Zr= 0.157), high $^{87}Sr/^{86}Sr$ and low $^{143}Nd/^{144}Nd$ (e.g., Peate et al., 2009).

569   Importantly, Stapafell continues the geochemical trends towards Iceland set by the Reykjanes Ridge

570   basalts in the direction of progressively enriched compositions. Trace element concentrations of the

571   Reykjanes Ridge basalts range between partial melts produced by DMM melting models and

572   Stapafell lavas (Fig. 9), indicating that the apparent influence of an enriched source on approach to

573   Iceland is possibly the same that supplies Stapafell.

574

575   The composition of one of the Reykjanes Ridge basalts closest to Iceland at ~400 km (185D4,

576   Table S2), displays one of the highest deviations of Fe^{3+}/Fe_{tot} and Nb/Zr from the predictions of the

577   DMM melting models. The chemistry of 185D4 glass can be envisaged as a mixture of two melts,

578   one produced from ambient DMM and one from the enriched source of Stapafell lavas. This

579   simplification allows the composition of the enriched melt portion for sample 185D4 to be

580   calculated through mass balance, using the chemical composition of a Reykjanes Ridge basalt not

581   influenced by the plume (e.g., sample 12aD1 at ~1100 km; Table S2) as the melt produced by

582   melting DMM and normalizing the contributions from each melt to the crustal thickness. The

583   enriched melt composition calculated following this approach has a REE pattern that is similar to

584   Stapafell basalt (Fig. 10), also validating the choice of Stapafell to investigate enrichment along the

585   Reykjanes Ridge.

586

587   Pyroxenite melting models conducted here can reproduce some of the trace element contents of

588   Stapafell lavas (Table S5), suggesting that KG1 pyroxenite or similar lithologies may cause the

589   trace element enrichment towards Iceland, in agreement with Shorttle and Maclennan (2011). Low-

590   degree melts (F= 4-10 %) have Fe^{3+}/Fe_{tot}= 0.159-0.176, which if mixed with melts produced by

591   melting DMM, in a 1:1 ratio, replicate the Fe^{3+}/Fe_{tot} of the Reykjanes Ridge basalts at 400 km from

592   Iceland. The models developed in this study confirm the increasing contribution from a pyroxenitic

593   rich source towards Iceland along the Reykjanes Ridge, which increases incompatible trace element

594   concentrations and is required to counterbalance the modelled decreasing Fe^{3+}/Fe_{tot} of the basalts

595   from a DMM source.

596

597   **5. Conclusions**

598   The behavior of V isotopes, V/Sc and Fe^{3+}/Fe_{tot} in the Reykjanes Ridge basalts can be summarized

599   as follow:

600

601   1. Vanadium isotopic compositions do not systematically vary along the Reykjanes Ridge ($\delta^{51}V$= -

602   0.97‰ ±0.17, n=19). $\delta^{51}V$ is not sensitive to the small fO_2 differences observed along the

603   Reykjanes Ridge but may be controlled by the extent of melting when compared with global

604   decompression melts (Wu et al., 2018). More studies on pristine basalts equilibrated at more

605   extreme fO_2 conditions than those recorded along the Reykjanes Ridge are required to investigate

606   the sensitivity of V isotopes to mantle fO_2. Vanadium isotopes appear insensitive to the presence

607   of pyroxenite in the Reykjanes Ridge mantle source.

608

609   2. V/Sc ratios show a general increase towards Iceland due to fractional crystallization of

610   clinopyroxene. High MgO basalts (> 7.5 wt%) not altered by crystallization show a minor

611   decrease of V/Sc ratios along the Reykjanes Ridge towards Iceland that agree with melts

612   produced by DMM melting models. However, V/Sc in the Reykjanes Ridge basalts does not

613   increase towards Iceland where enriched and more oxidized mantle source is sampled by the

614   basalts, suggesting that this proxy is not responsive to the presence of mantle chemical

615   heterogeneities in these samples. The use of V/Sc as a fO_2 proxy is highly model-dependent,

616   requiring independent constraints on source mineralogy, trace element abundance, extent of

617   melting, and Tp. These parameters for Reykjanes Ridge lavas are sufficiently uncertain at this

618   time to permit non-unique fO_2 determinations from measured V/Sc ratios.

619

3. Recalibrated Fe^{3+}/Fe_{tot} ratios, corrected for fractionation (MgO_{10}), remain virtually constant along the Reykjanes Ridge. Thermodynamic melting models of DMM can reproduce Reykjanes Ridge Fe^{3+} contents between 1100 and 700 km from the plume. However, melts produced upon melting DMM need to be mixed with melts formed from an enriched source close to the plume, such as pyroxenite, to replicate the Fe^{3+}/Fe_{tot} ratios observed between 400 and 700 km, which would otherwise decrease under the influence of increased mantle potential temperature. Basalt Fe^{3+}/Fe_{tot} both depends on melting conditions (T_p) and is responsive to bulk oxidation state alterations associated with the presence of chemical heterogeneities in the mantle.

References

Asimow, P.D., Ghiorso, M.S., 1998. Algorithmic modifications extending MELTS to calculate subsolidus phase relations. Am. Mineral. 83, 1127–1132. https://doi.org/10.2138/am-1998-9-1022

Bach, W., Bernhard, P.E., Hart, S.R., Blusztajn, J.S., 2003. Geochemistry of hydrothermally altered oceanic crust: DSDP/ODP Hole 504B-Implications for seawater-crust exchange budgets and Sr-and Pb-isotopic evolution of the mantle. Geochemistry, Geophys. Geosystems 4, 40–55.

646   https://doi.org/10.1029/2002GC000419

647   Berry, A.J., Stewart, G.A., O'Neill, H.S.C., Mallmann, G., Mosselmans, J.F.W., 2018. A re-

648   assessment of the oxidation state of iron in MORB glasses. Earth Planet. Sci. Lett. 483, 114–

649   123. https://doi.org/10.1016/j.epsl.2017.11.032

650   Birner, S.K., Cottrell, E., Warren, J.M., Kelley, K.A., Davis, F.A., 2018. Peridotites and basalts

651   reveal broad congruence between two independent records of mantle fO2 despite local redox

652   heterogeneity. Earth Planet. Sci. Lett. 494, 172–189. https://doi.org/10.1016/j.epsl.2018.04.035

653   Brounce, M., Kelley, K.A., Cottrell, E., Reagan, M.K., 2015. Temporal evolution of mantle wedge

654   oxygen fugacity during subduction initiation. Geology 43, 775–778.

655   https://doi.org/10.1130/G36742.1

656   Brounce, M., Stolper, E., Eiler, J., 2017. Redox variations in Mauna Kea lavas, the oxygen fugacity

657   of the Hawaiian plume, and the role of volcanic gases in Earth's oxygenation. Proc. Natl.

658   Acad. Sci. 114, 8997–9002. https://doi.org/10.1073/pnas.1619527114

659   Brounce, M.N., Kelley, K.A., Cottrell, E., 2014. Variations in Fe3+/PFe of Mariana Arc Basalts and

660   MantleWedge fO2. J. Petrol. 55, 2514–2536. https://doi.org/10.1093/petrology/egu065

661   Bucholz, C.E., Kelemen, P.B., 2019. Oxygen fugacity at the base of the Talkeetna arc, Alaska.

662   Contrib. to Mineral. Petrol. 174, 1–27. https://doi.org/10.1007/s00410-019-1609-z

663   Canil, D., 1999. Vanadium partitioning between orthopyroxene, spinel and silicate melt and the

664   redox states of mantle source regions for primary magmas. Geochim. Cosmochim. Acta 63,

665   557–572. https://doi.org/10.1016/S0016-7037(98)00287-7

666   Canil, D., 1997. Vanadium partitioning and the oxidation state of Archaean komatiite magmas.

667   Nature 389, 842–845.

668   Canil D., O'Neill H. C., 1996. Distribution of Ferric Iron in some Upper-Mantle Assemblages . J.

669   Petrol. 37, 609–635.

670   Cottrell, E., Kelley, K.A., 2013. Redox heterogeneity in mid-ocean ridge basalts as a function of

671   mantle source. Science 340, 1314–1317. https://doi.org/10.1126/science.1233299

672   Cottrell, E., Kelley, K.A., 2011. The oxidation state of Fe in MORB glasses and the oxygen

673   fugacity of the upper mantle. Earth Planet. Sci. Lett. 305, 270–282.

674   https://doi.org/10.1016/j.epsl.2011.03.014

675   Cottrell, E., Kelley, K.A., Lanzirotti, A., Fischer, R.A., 2009. High-precision determination of iron

676   oxidation state in silicate glasses using XANES. Chem. Geol. 268, 167–179.

677   https://doi.org/10.1016/j.chemgeo.2009.08.008

678   Davis, F.A., Cottrell, E., 2018. Experimental investigation of basalt and peridotite oxybarometers:

679   Implications for spinel thermodynamic models and Fe3+ compatibility during generation of

680   upper mantle melts. Am. Mineral. 103, 1056–1067. https://doi.org/10.2138/am-2018-6280

681   Frost, D.J., McCammon, C.A., 2008. The Redox State of Earth's Mantle. Annu. Rev. Earth Planet.

682   Sci. 36, 389–420. https://doi.org/10.1146/annurev.earth.36.031207.124322

683   Frost, R.B., 1991. Introduction to oxygen fugacity and its petrologic importance, in: Reviews in

684   Mineralogy & Geochemistry 25. pp. 1–10.

685   Gaetani, G.A., 2016. The behavior of Fe 3+ /∑Fe during partial melting of spinel lherzolite.

686   Geochim. Cosmochim. Acta 185, 64–77. https://doi.org/10.1016/j.gca.2016.03.019

687   Gaillard, F., Scaillet, B., Arndt, N.T., 2011. Atmospheric oxygenation caused by a change in

688   volcanic degassing pressure. Nature 478, 229–232. https://doi.org/10.1038/nature10460

689   Gale, A., Dalton, C.A., Langmuir, C.H., Su, Y., Schilling, J.G., 2013. The mean composition of

690   ocean ridge basalts, Geochemistry, Geophysics, Geosystems.

691   https://doi.org/10.1029/2012GC004334

692   Ghiorso, M.S., Hirschmann, M.M., Reiners, P.W., Kress, V.C., 2002. The pMELTS: A revision of

693   MELTS for improved calculation of phase relations and major element partitioning related to

694   partial melting of the mantle to 3 GPa. Geochemistry, Geophys. Geosystems 3, 1–35.

695   https://doi.org/10.1029/2001GC000217

696   Hartley, M.E., Shorttle, O., Maclennan, J., Moussallam, Y., Edmonds, M., 2017. Olivine-hosted

697   melt inclusions as an archive of redox heterogeneity in magmatic systems. Earth Planet. Sci.

698   Lett. 479, 192–205. https://doi.org/10.1016/j.epsl.2017.09.029

699 Helz, R.T., Cottrell, E., Brounce, M.N., Kelley, K.A., 2017. Olivine-melt relationships and

700   syneruptive redox variations in the 1959 eruption of Kīlauea Volcano as revealed by XANES.

701   J. Volcanol. Geotherm. Res. 333–334, 1–14. https://doi.org/10.1016/j.jvolgeores.2016.12.006

702 Hopkins, S.S., Prytulak, J., Barling, J., Russell, S.S., Coles, B.J., Halliday, A.N., 2019. The

703   vanadium isotopic composition of lunar basalts. Earth Planet. Sci. Lett. 511, 12–24.

704   https://doi.org/10.1016/j.epsl.2019.01.008

705 Jones, S.M., Murton, B.J., Fitton, J.G., White, N.J., Maclennan, J., Walters, R.L., 2014. A joint

706   geochemical-geophysical record of time-dependent mantle convection south of Iceland. Earth

707   Planet. Sci. Lett. 386, 86–97. https://doi.org/10.1016/j.epsl.2013.09.029

708 Kelley, K.A., Cottrell, E., 2012. The influence of magmatic differentiation on the oxidation state of

709   Fe in a basaltic arc magma. Earth Planet. Sci. Lett. 329–330, 109–121.

710   https://doi.org/10.1016/j.epsl.2012.02.010

711 Kelley, K.A., Cottrell, E., 2009. Water and the oxidation state of subduction zone magmas. Science

712   325, 605–607.

713 Klein, E.M., Langmuir, C.H., 1987. Global Correlations of Ocean Ridge Basalt Chemistry with

714   Axial Depth and Crustal Thickness. J. Geophys. Res. 92, 8089–8115.

715 Kogiso, T., Hirose, K., Takahashi, E., 1998. Melting experiments on homogeneous mixtures of

716   peridotite and basalt: Application to the genesis of ocean island basalts. Earth Planet. Sci. Lett.

717   162, 45–61. https://doi.org/10.1016/S0012-821X(98)00156-3

718 Kress, V.C., Carmichael, I.S.E., 1991. The compressibility of silicate liquids containing Fe_2O_3 and

719   the effect of composition, temperature, oxygen fugacity and pressure on their redox state.

720   Contrib. to Mineral. Petrol. 108, 82–92.

721 Laubier, M., Grove, T.L., Langmuir, C.H., 2014. Trace element mineral/melt partitioning for

722   basaltic and basaltic andesitic melts: An experimental and laser ICP-MS study with application

723   to the oxidation state of mantle source regions. Earth Planet. Sci. Lett. 392, 265–278.

28

724 https://doi.org/10.1016/j.epsl.2014.01.053

725 Lee, C.T.A., Brandon, A.D., Norman, M., 2003. Vanadium in peridotites as a proxy for paleo-fO2

726 during partial melting: Prospects, limitations, and implications. Geochim. Cosmochim. Acta

727 67, 3045–3064. https://doi.org/10.1016/S0016-7037(00)00268-0

728 Lee, C.T.A., Leeman, W.P., Canil, D., Li, Z.X.A., 2005. Similar V/Sc systematics in MORB and

729 arc basalts: Implications for the oxygen fugacities of their mantle source regions. J. Petrol. 46,

730 2313–2336. https://doi.org/10.1093/petrology/egi056

731 Li, Z.X.A., Lee, C.T.A., 2004. The constancy of upper mantle fO 2 through time inferred from V/Sc

732 ratios in basalts. Earth Planet. Sci. Lett. 228, 483–493.

733 https://doi.org/10.1016/j.epsl.2004.10.006

734 Mallmann, G., O'Neill, H.S.C., 2013. Calibration of an empiricalthermometer and oxybarometer

735 based on the partitioning of sc, Y and V between olivine and silicate melt. J. Petrol. 54, 933–

736 949. https://doi.org/10.1093/petrology/egt001

737 Mallmann, G., O'Neill, H.S.C., 2009. The crystal/melt partitioning of V during mantle melting as a

738 function of oxygen fugacity compared with some other elements (Al, P, Ca, Sc, Ti, Cr, Fe, Ga,

739 Y, Zr and Nb). J. Petrol. 50, 1765–1794. https://doi.org/10.1093/petrology/egp053

740 Matthews, S., Shorttle, O., Maclennan, J., 2016. The temperature of the Icelandic mantle from

741 olivine-spinel aluminum exchange thermometry. Geochemistry Geophys. Geosystems 17,

742 4725–4752. https://doi.org/10.1002/ 2016GC006497

743 Mckenzie, D., O'nions, R.K., 1995. The source regions of ocean island basalts. J. Petrol. 36, 133–

744 159. https://doi.org/10.1093/petrology/36.1.133

745 McKenzie, D., O'Nions, R.K., 1991. Partial melt coefficients from inversion of rare earth element

746 concentrations. J. Petrol. 23, 1021–1091.

747 https://doi.org/http://dx.doi.org/10.1093/petrology/32.5.1021

748 Moussallam, Y., Edmonds, M., Scaillet, B., Peters, N., Gennaro, E., Sides, I., Oppenheimer, C.,

749 2016. The impact of degassing on the oxidation state of basaltic magmas: A case study of

750 Kīlauea volcano. Earth Planet. Sci. Lett. 450, 317–325.

751 https://doi.org/10.1016/j.epsl.2016.06.031

752 Moussallam, Y., Oppenheimer, C., Scaillet, B., Gaillard, F., Kyle, P., Peters, N., Hartley, M., Berlo,

753 K., Donovan, A., 2014. Tracking the changing oxidation state of Erebus magmas, from mantle

754 to surface, driven by magma ascent and degassing. Earth Planet. Sci. Lett. 393, 200–209.

755 https://doi.org/10.1016/j.epsl.2014.02.055

756 Murton, B.J., Taylor, R.N., Thirlwall, M.F., 2002. Plume-Ridge Interaction: a Geochemical

757 Perspective from the Reykjanes Ridge. J. Petrol. 43, 1987–2012.

758 https://doi.org/10.1093/petrology/43.11.1987

759 Nielsen, S.G., Prytulak, J., Halliday, A.N., 2011. Determination of Precise and Accurate 51V/50V

760 Isotope Ratios by MC-ICP-MS, Part 1: Chemical Separation of Vanadium and Mass

761 Spectrometric Protocols. Geostand. Geoanalytical Res. 35, 293–306.

762 https://doi.org/10.1111/j.1751-908x.2011.00106.x

763 O'Neill, H.S.C., Berry, A.J., Mallmann, G., 2018. The oxidation state of iron in Mid-Ocean Ridge

764 Basaltic (MORB) glasses: Implications for their petrogenesis and oxygen fugacities. Earth

765 Planet. Sci. Lett. 504, 152–162. https://doi.org/10.1016/j.epsl.2018.10.002

766 O'Neill, H.S.C., Wall, V.J., 1987. The olivine-orthopyroxene-spinel oxygen geobarometer, the

767 nickel precipitation curve, and the oxygen fugacity of the earth's upper mantle. J. Petrol. 28,

768 1169–1191.

769 Peate, D.W., Baker, J.A., Jakobsson, S.P., Waight, T.E., Kent, A.J.R., Grassineau, N. V.,

770 Skovgaard, A.C., 2009. Historic magmatism on the Reykjanes Peninsula, Iceland: A snap-shot

771 of melt generation at a ridge segment. Contrib. to Mineral. Petrol. 157, 359–382.

772 https://doi.org/10.1007/s00410-008-0339-4

773 Prytulak, J., Nielsen, S.G., Ionov, D.A., Halliday, A.N., Harvey, J., Kelley, K.A., Niu, Y.L., Peate,

774 D.W., Shimizu, K., Sims, K.W.W., 2013. The stable vanadium isotope composition of the

775 mantle and mafic lavas. Earth Planet. Sci. Lett. 365, 177–189.

776   https://doi.org/10.1016/j.epsl.2013.01.010

777   Prytulak, J., Sossi, P.A., Halliday, A.N., Plank, T., Savage, P.S., Woodhead, J.D., 2017. Stable

778   vanadium isotopes as a redox proxy in magmatic systems? Geochemical Perspect. Lett. 75–84.

779   https://doi.org/10.7185/geochemlet.1708

780   Rouxel, O., Dobbek, N., Ludden, J., Fouquet, Y., 2003. Iron isotope fractionation during oceanic

781   crust alteration. Chem. Geol. 202, 155–182. https://doi.org/10.1016/j.chemgeo.2003.08.011

782   Rudge, J.F., Maclennan, J., Stracke, A., 2013. The geochemical consequences of mixing melts from

783   a heterogeneous mantle. Geochim. Cosmochim. Acta 114, 112–143.

784   https://doi.org/10.1016/j.gca.2013.03.042

785   Salters, V.J.M., Stracke, A., 2004. Composition of the depleted mantle. Geochemistry, Geophys.

786   Geosystems 5. https://doi.org/10.1029/2003GC000597

787   Schilling, JG, 1973. Iceland Mantle Plume: Geochemical study of Reykjanes Ridge. Nature 242,

788   565–571.

789   Shorttle, O., Maclennan, J., 2011. Compositional trends of Icelandic basalts: Implications for short-

790   length scale lithological heterogeneity in mantle plumes. Geochemistry, Geophys. Geosystems

791   12. https://doi.org/10.1029/2011GC003748

792   Shorttle, O., MacLennan, J., Jones, S.M., 2010. Control of the symmetry of plume-ridge interaction

793   by spreading ridge geometry. Geochemistry, Geophys. Geosystems 11, 1–27.

794   https://doi.org/10.1029/2009GC002986

795   Shorttle, O., Moussallam, Y., Hartley, M.E., Maclennan, J., Edmonds, M., Murton, B.J., 2015. Fe-

796   XANES analyses of Reykjanes Ridge basalts: Implications for oceanic crust's role in the solid

797   Earth oxygen cycle. Earth Planet. Sci. Lett. 427, 272–285.

798   https://doi.org/10.1016/j.epsl.2015.07.017

799   Sims, K.W.W., Depaolo, D.J., Murrell, M.T., Baldridge, W.S., Goldstein, S., Clague, D., Jull, M.,

800   1999. Porosity of the melting zone and variations in the solid mantle upwelling rate beneath

801   Hawaii: Inferences from 238U-230Th-226Ra and 235U-231Pa disequilibria. Geochim.

802   Cosmochim. Acta 63, 4119–4138.

803   Smith, P.M., Asimow, P.D., 2005. Adiabat-1ph: A new public front-end to the MELTS, pMELTS,

804   and pHMELTS models. Geochemistry, Geophys. Geosystems 6, 1–8.

805   https://doi.org/10.1029/2004GC000816

806   Sossi, P.A., Prytulak, J., O'Neill, H.S.C., 2018. Experimental calibration of vanadium partitioning

807   and stable isotope fractionation between hydrous granitic melt and magnetite at 800 °C and

808   0.5 GPa. Contrib. to Mineral. Petrol. 173, 0. https://doi.org/10.1007/s00410-018-1451-8

809   Stolper, D.A., Keller, C.B., 2018. A record of deep-ocean dissolved O2 from the oxidation state of

810   iron in submarine basalts. Nature 553, 323–327. https://doi.org/10.1038/nature25009

811   Stracke, A., Bizimis, M., Salters, V.J.M., 2003. Recycling oceanic crust: Quantitative constraints.

812   Geochemistry, Geophys. Geosystems 4. https://doi.org/10.1029/2001GC000223

813   Teng, F.-Z., Dauphas, N., Watkins, J.M., 2017. Non-Traditional Stable Isotopes: Retrospective and

814   Prospective, in: Reviews in Mineralogy & Geochemistry. pp. 1–26.

815   https://doi.org/10.2138/rmg.2017.82.1

816   Workman, R.K., Hart, S.R., 2005. Major and trace element composition of the depleted MORB

817   mantle (DMM). Earth Planet. Sci. Lett. 231, 53–72. https://doi.org/10.1016/j.epsl.2004.12.005

818   Wu, F., Qi, Y., Perfit, M.R., Gao, Y., Langmuir, C.H., Wanless, V.D., Yu, H., Huang, F., 2018.

819   Vanadium isotope compositions of mid-ocean ridge lavas and altered oceanic crust. Earth

820   Planet. Sci. Lett. 493, 128–139. https://doi.org/10.1016/j.epsl.2018.04.009

821   Zhang, H.L., Cottrell, E., Solheid, P.A., Kelley, K.A., Hirschmann, M.M., 2018. Determination of

822     $Fe^{3+}/\Sigma Fe$ of XANES basaltic glass standards by Mössbauer spectroscopy and its application

823   to the oxidation state of iron in MORB. Chem. Geol. 479, 166–175.

824   https://doi.org/10.1016/j.chemgeo.2018.01.006

825   Zhang, H.L., Hirschmann, M.M., Cottrell, E., Newville, M., Lanzirotti, A., 2016. Structural

826   environment of iron and accurate determination of $Fe^{3+}/\sigma Fe$ ratios in andesitic glasses by

827   XANES and Mössbauer spectroscopy. Chem. Geol. 428, 48–58.

829

830   **Figure captions**

831   **Fig. 1**: Map showing the location of the Reykjanes Ridge basalts investigated in this study (dark

832   blue circles indicating samples with Fe^{3+}/Fe_{tot} and V/Sc data, light blue circles showing those with

833   additional V isotopic compositions). Stapafell eruption on the Reykjanes Peninsula (coral circle)

834   and the plume center location (white star) proposed by Shorttle et al. (2010) are also shown. The

835   map was prepared with the software GeoMapApp (www.geomapapp.org).

836

837   **Fig. 2**: Vanadium isotopes along the investigated spread of the Reykjanes Ridge, reported as $\delta^{51}V$,

838   plotted as a function of MgO content (Shorttle et al., 2015). The grey horizontal bar indicates the

839   average MORB value of Wu et al. (2018) with calculated 2SD.

840

841   **Fig.3**: Vanadium isotopic composition plotted against (**a**) Fe^{3+}/Fe_{tot} (corrected to MgO_{10}, see text)

842   and (**b**) V/Sc. Circles are color coded as a function of MgO content measured by electron

843   microprobe (Shorttle et al., 2015).

844

845   **Fig. 4**: Na_8 vs $\delta^{51}V$ of the Reykjanes Ridge lavas investigated in this study (circles). Ridge

846   segments data from Wu et al. (2018) and Prytulak et al. (2013) are also plotted as diamonds (Na_8

847   data reported in Wu et al., 2018). Na_8 values for the Reykjanes Ridge samples were calculated from

848   the regressed melt compositions at ~8 wt% MgO (see text) using the formula of Shorttle et al.

849   (2010). The grey horizontal bar indicates the average MORB value of Wu et al. (2018) with

850   calculated 2SD.

851

852   **Fig. 5**: The V/Sc ratio of the Reykjanes Ridge basalts as a function of distance from the Icelandic

853   plume. Samples are color coded with the MgO content (Shorttle et al., 2015), highlighting the effect

854 of fractional crystallization. Errors of the V/Sc ratios were calculated from the errors on V and Sc

855 (LA-ICPMS analyses; Supplementary Table S2) and range between 0.11 and 1.29 1SD.

856

857 **Fig. 6**: CaO vs MgO content of the Reykjanes Ridge basalts as a function of V/Sc ratio.

858

859 **Fig. 7**: Fe^{3+}/Fe_{tot} ratio and oxygen fugacity along the Reykjanes Ridge. (**a**) Raw Fe^{3+}/Fe_{tot} ratios

860 recalculated from the study of Shorttle et al. (2015) using the new calibration of the XANES

861 standards (Zhang et al., 2018; see text). Data are plotted as a function of MgO content of the glasses

862 (Shorttle et al., 2015). (**b**) Fe^{3+}/Fe_{tot} ratios of the same samples in (**a**) but now corrected for

863 fractional crystallization to MgO_{10} (see text), as a function of Nb/Zr. (**c**) Oxygen fugacity, as $\log fO_2$

864 relative to the FMQ buffer (Frost, 1991), calculated from the data in (**b**) using the calibration of

865 Kress and Carmichael (1991) at 2 kb and 1200 °C. Data are plotted as a function of Nb/Zr of the

866 glasses.

867

868 **Fig. 8**: Reykjanes Ridge basalt (blue circles) plotted as a function of distance from the Icelandic

869 plume along with partial melt compositions produced by the thermodynamic melting models of

870 DMM with 4, 5 and 6% Fe^{3+}/Fe_{tot} in the source (grey circles). (**a**) Fe^{3+}/Fe_{tot} ratios of basalt corrected

871 to MgO_{10}. (**b**) V/Sc ratios, where light blue circles indicate more evolved basalts (< 7.5 wt% MgO)

872 and dark blue circles indicate more primitive compositions (> 7.5 wt% MgO). (**c**) Nb/Zr ratios, with

873 concentrations of the different models overlapping and being indistinguishable at the scale of the

874 plot. Pale red arrows in panel (**a**) and (**c**) highlight the disparity between Reykjanes Ridge basalts

875 and DMM modelled compositions near Iceland.

876

877 **Fig. 9**: Ba and La compositional trend of Reykjanes Ridge basalts (blue) between partial melts

878 produced by DMM melting model with 5% initial Fe^{3+}/Fe_{tot} (grey) and Stapafell basalt from the

879 Reykjanes Peninsula (coral).

880

Fig. 10: Spider diagram reporting the trace element composition of Stapafell basaltic glass (Peate et al., 2009), in coral, and the enriched melt forming at the point closest to the Icelandic plume along the Reykjanes Ridge, in blue. In grey and yellow are also represented the compositions of Reykjanes Ridge basalts 12aD1 (~1100 from Iceland) and 185D4 (~ 400 km from Iceland), respectively, used to mass balance the enriched melt composition. See text for more details.

886

Fig. S1: Fractional crystallization model for Reykjanes Ridge basalt 153D3. The melt concentration was calculated at an arbitrary low pressure of 0.6 kb using MELTS (Ghiorso et al., 2002; Smith and Asimow, 2005). The model shows that V/Sc ratios in melts with MgO >7.5 wt% are not affected by crystallization. Calculations employed D_V and D_{Sc} at FMQ from Mallmann and O'Neill (2009, 2013). Between 9 and 7.5 wt% MgO only olivine crystallizes, while clinopyroxene (cpx) and plagioclase (plag) start to crystallize at ~7.5 and ~6 wt% MgO, respectively.

893

Fig. S2: Difference in Fe^{3+}/Fe_{tot} between the Reykjanes Ridge basalt and the partial melt composition produced by DMM melting model with 5% initial Fe^{3+}/Fe_{tot} ($\Delta Fe^{3+}/Fe_{tot}$), calculated at a particular distance, against the Nb/Zr ratio of the Reykjanes Ridge basalts.
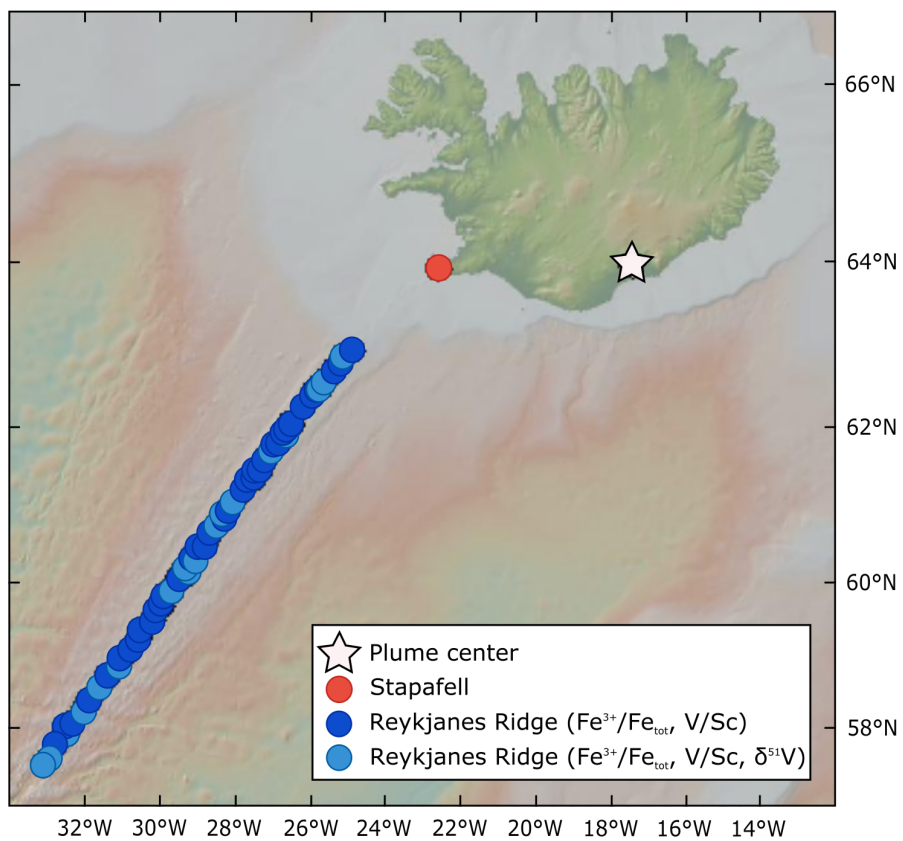
(a) Plot of $\delta^{51}V_{AA}$ versus Fe^{3+}/Fe_{tot}, colored by MgO.

(b) Plot of $\delta^{51}V_{AA}$ versus V/Sc, colored by MgO.
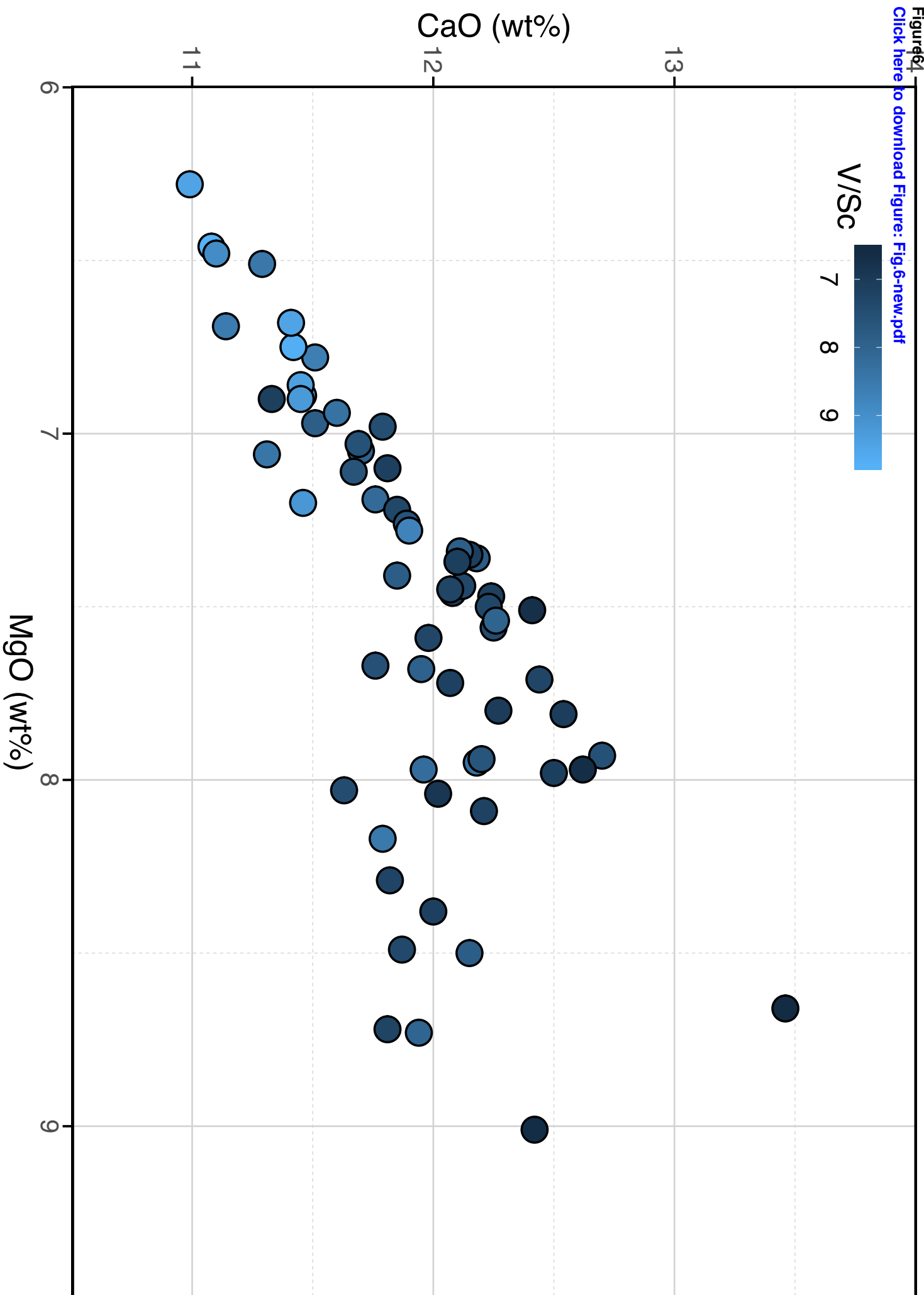
Figure4_0.4
Click here to download Figure: Fig.-4-new.pdf
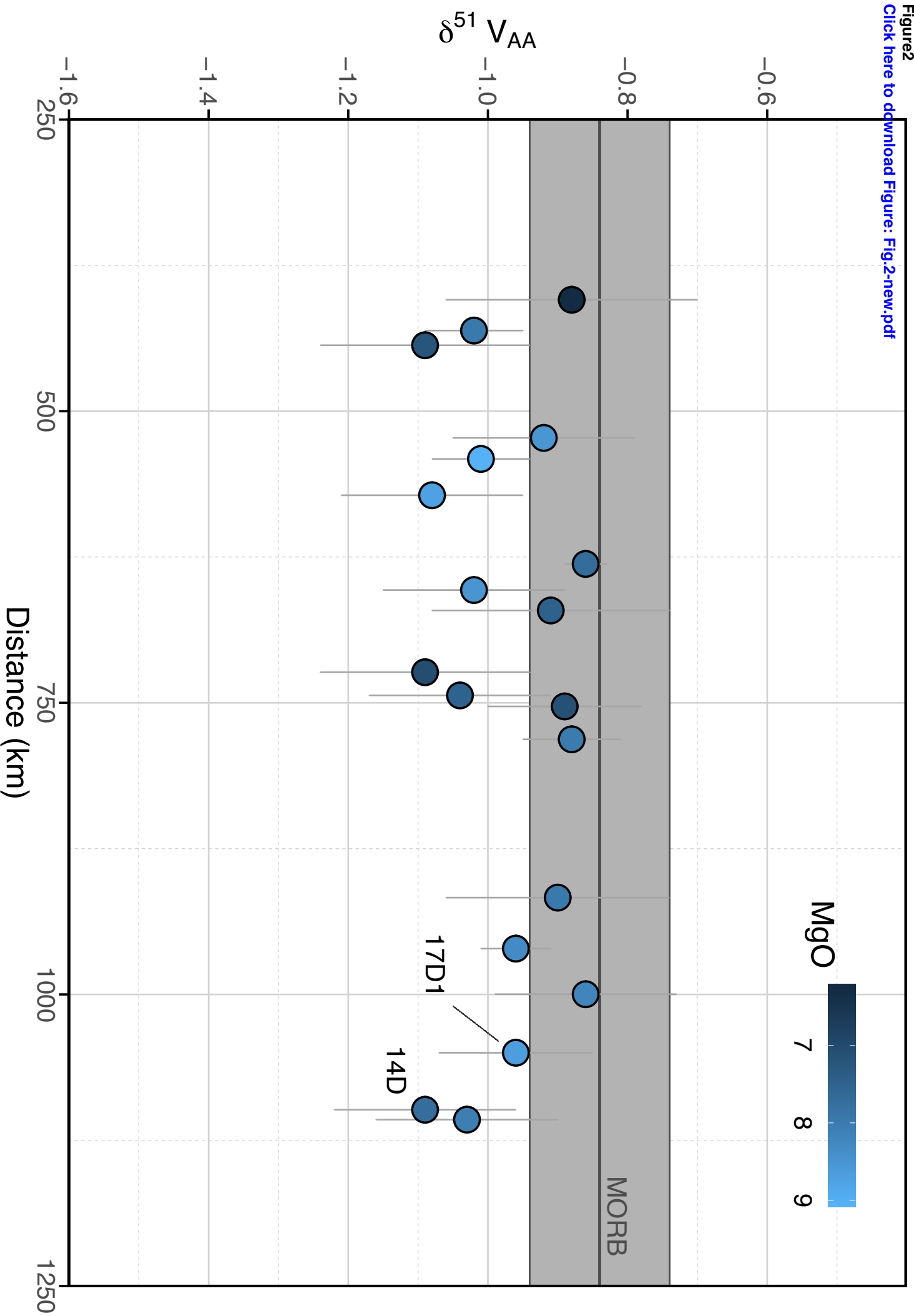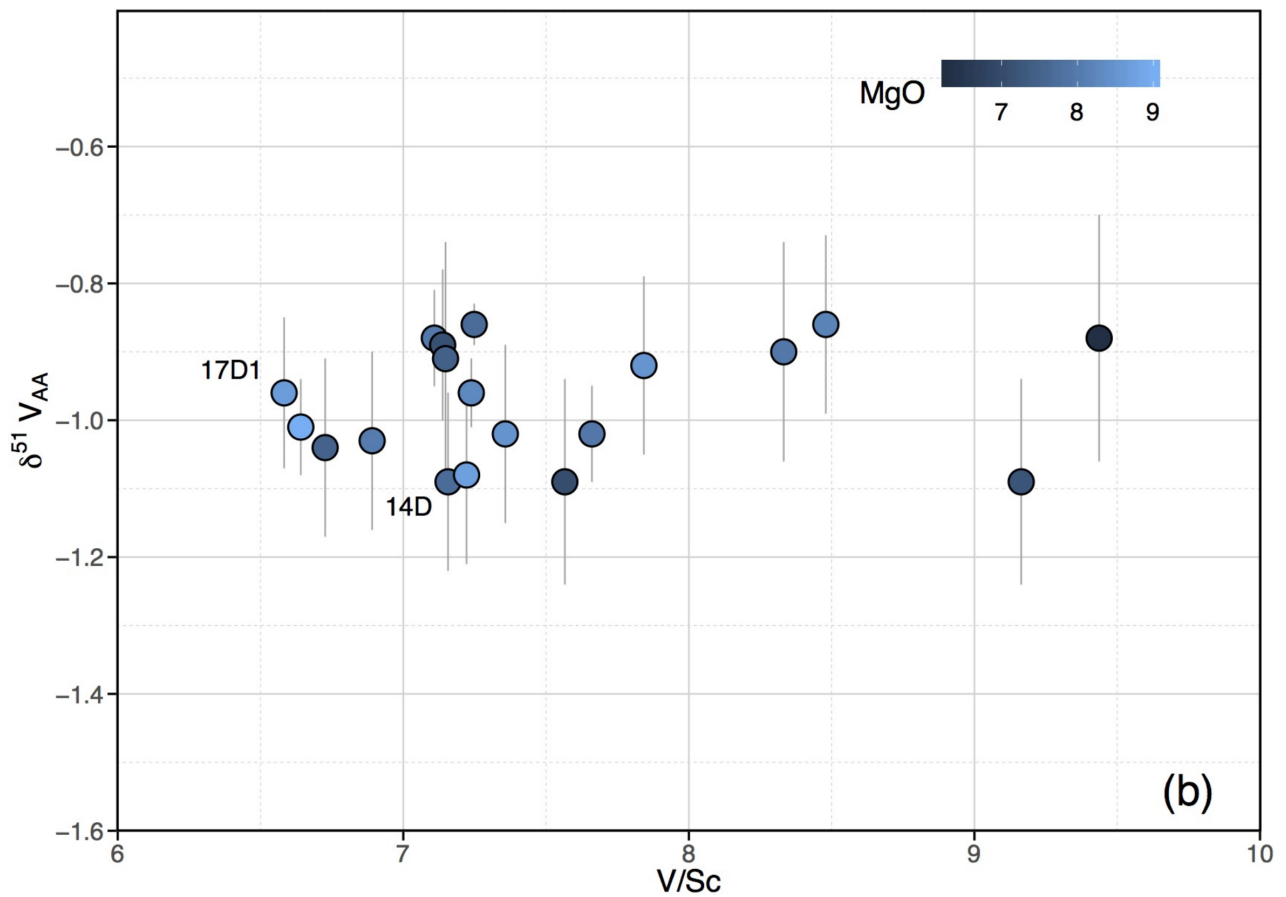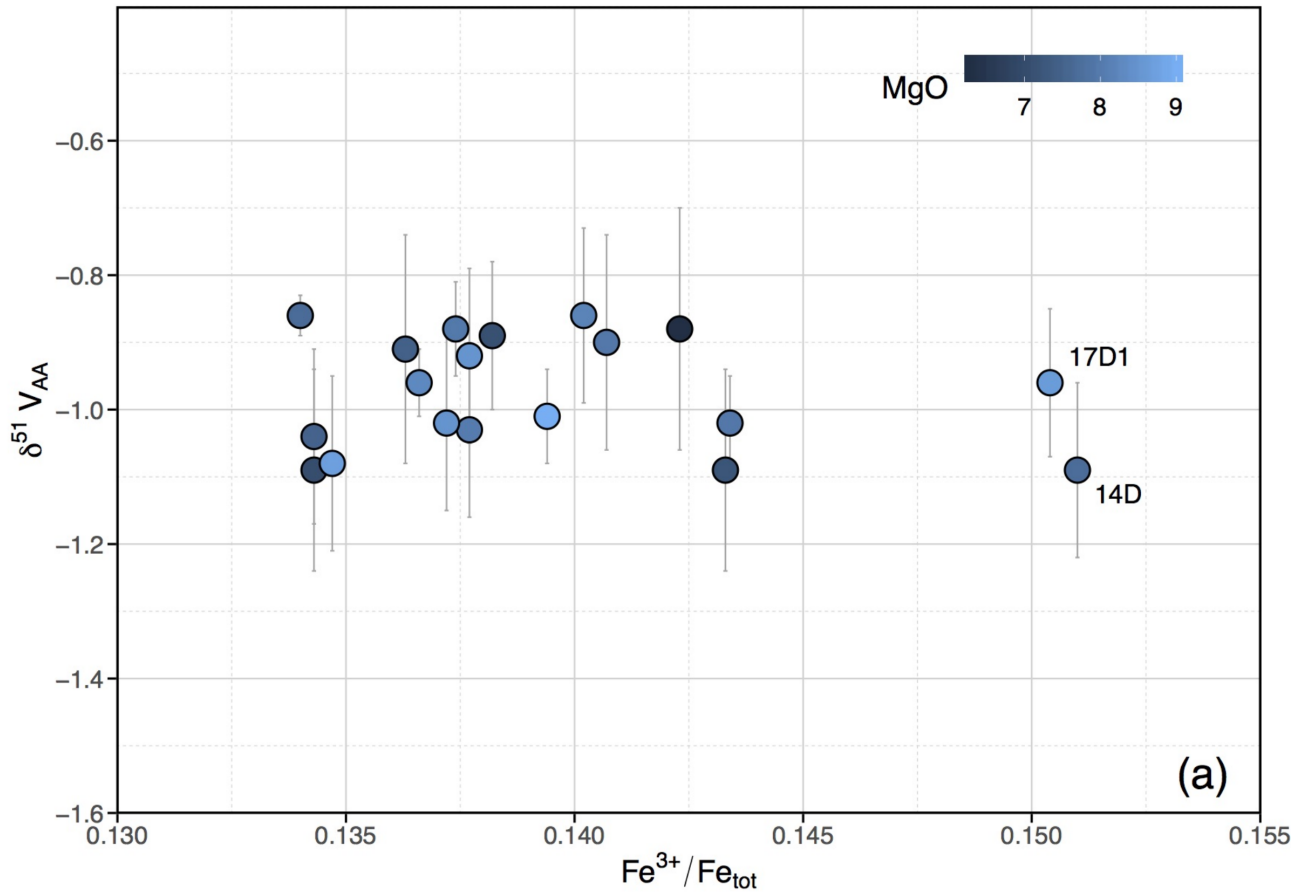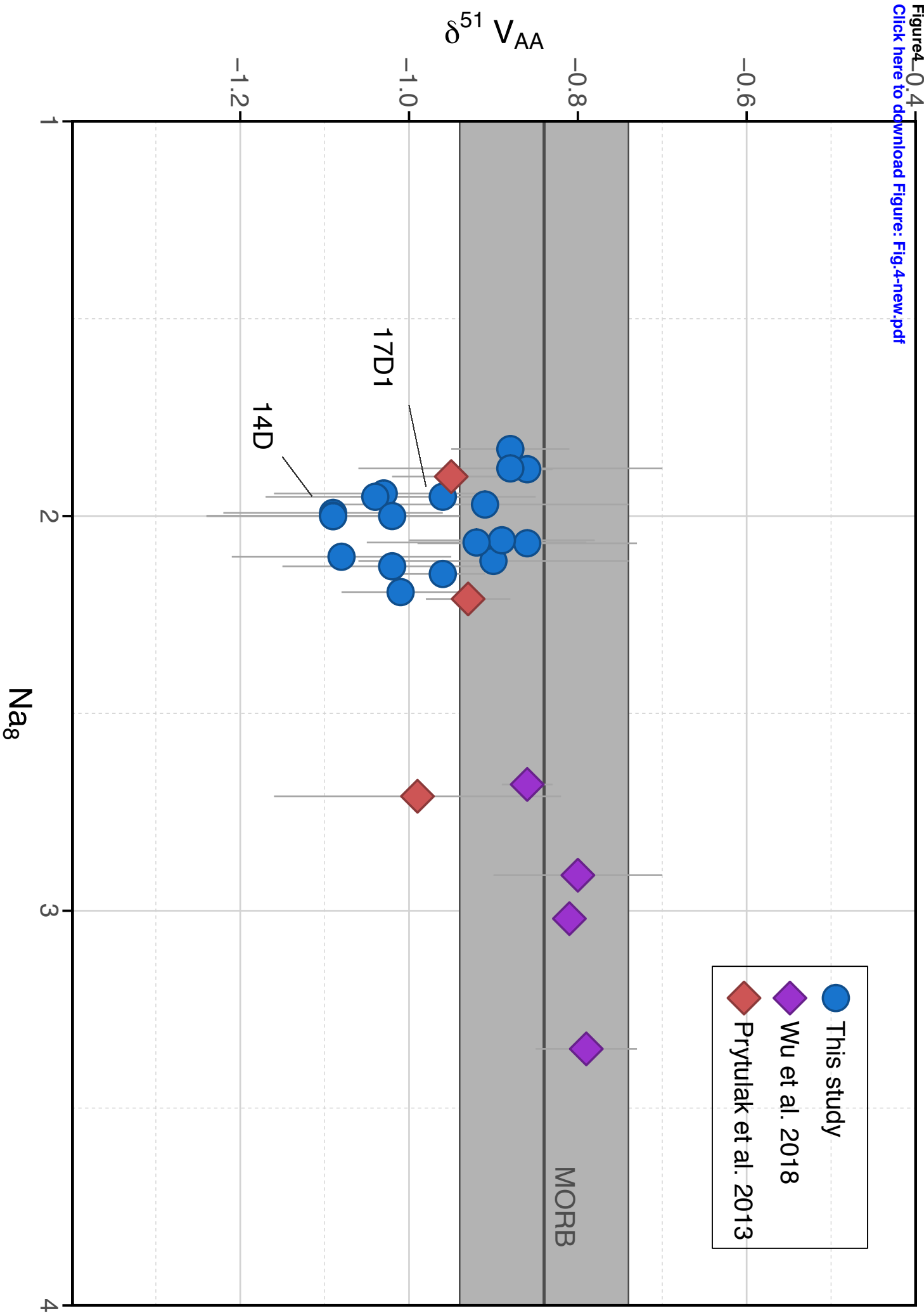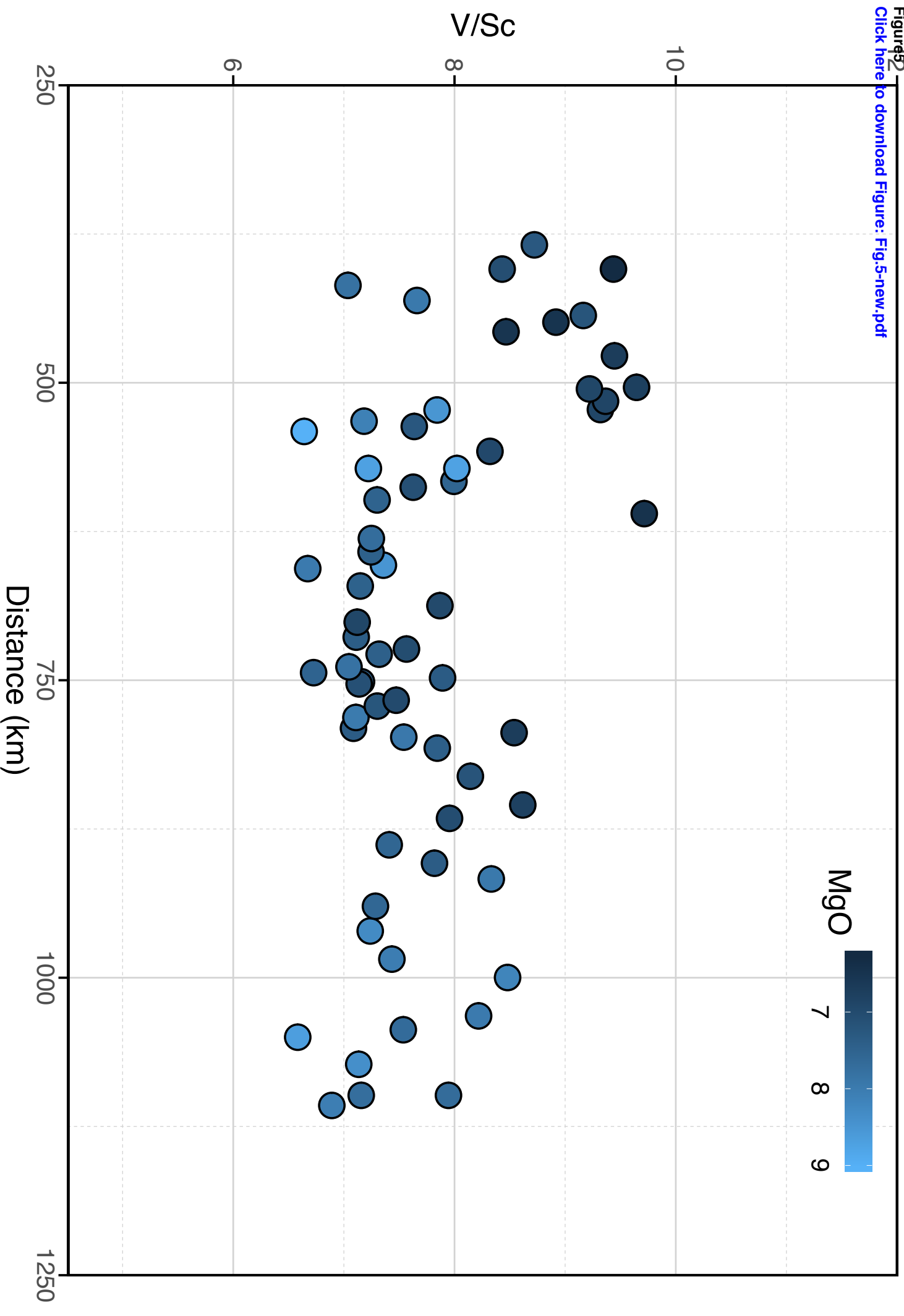
Figure 6

Figure7
Click here to download Figure: Fig.7-new.pdf

(a)

(b)

(c)
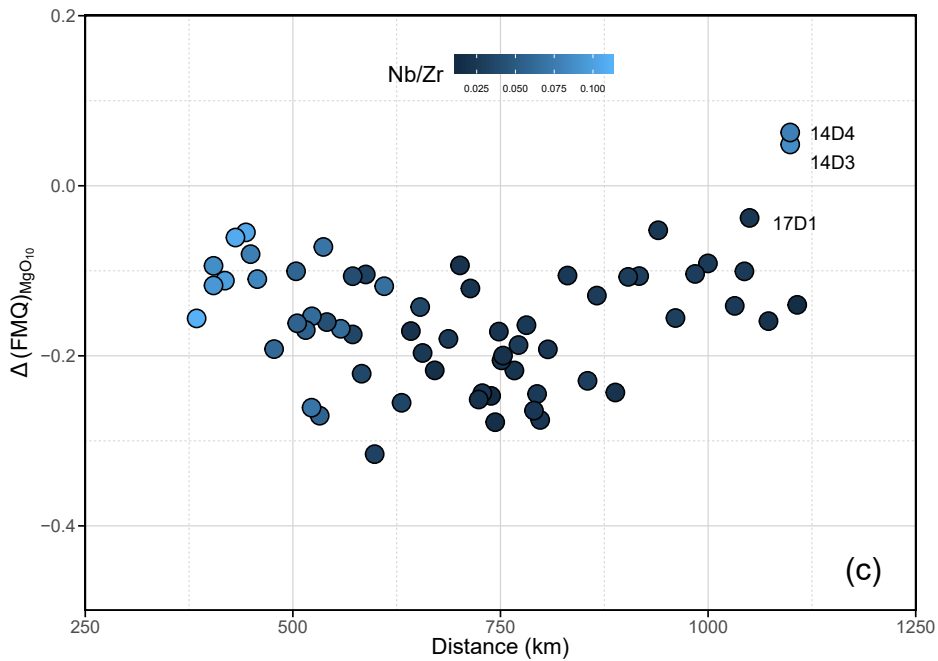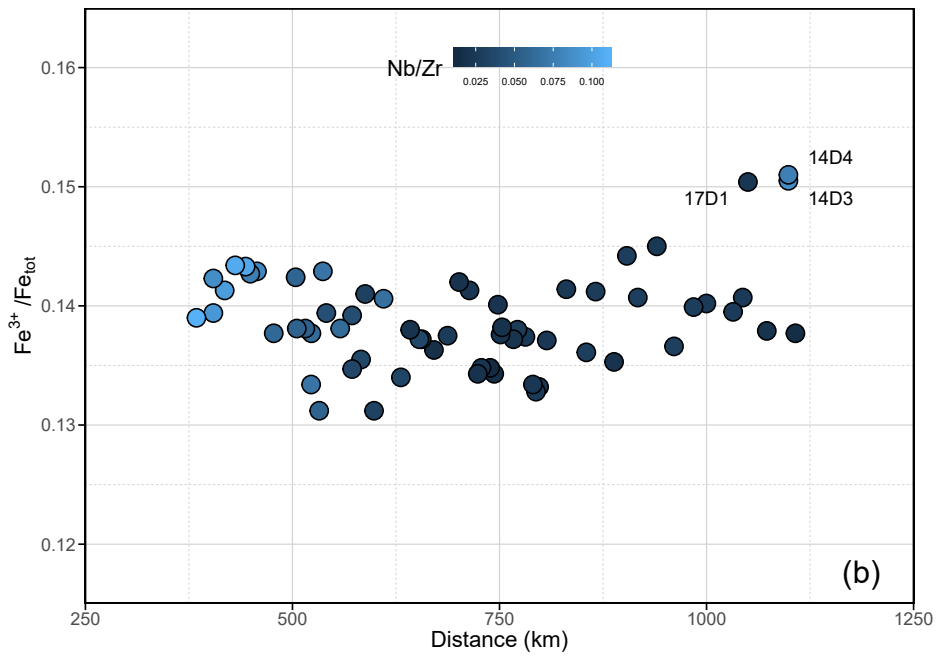
Figure8
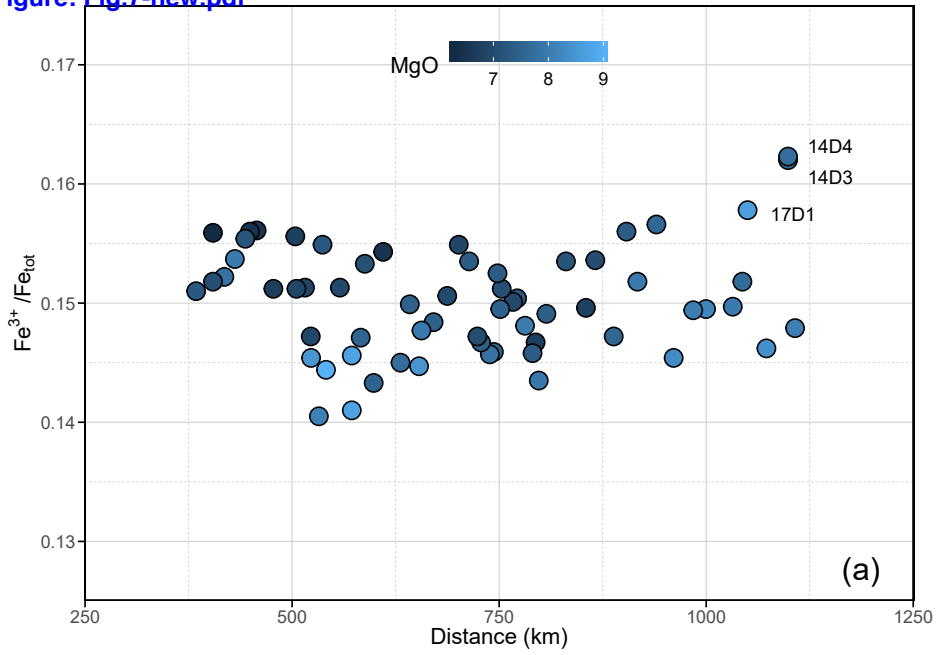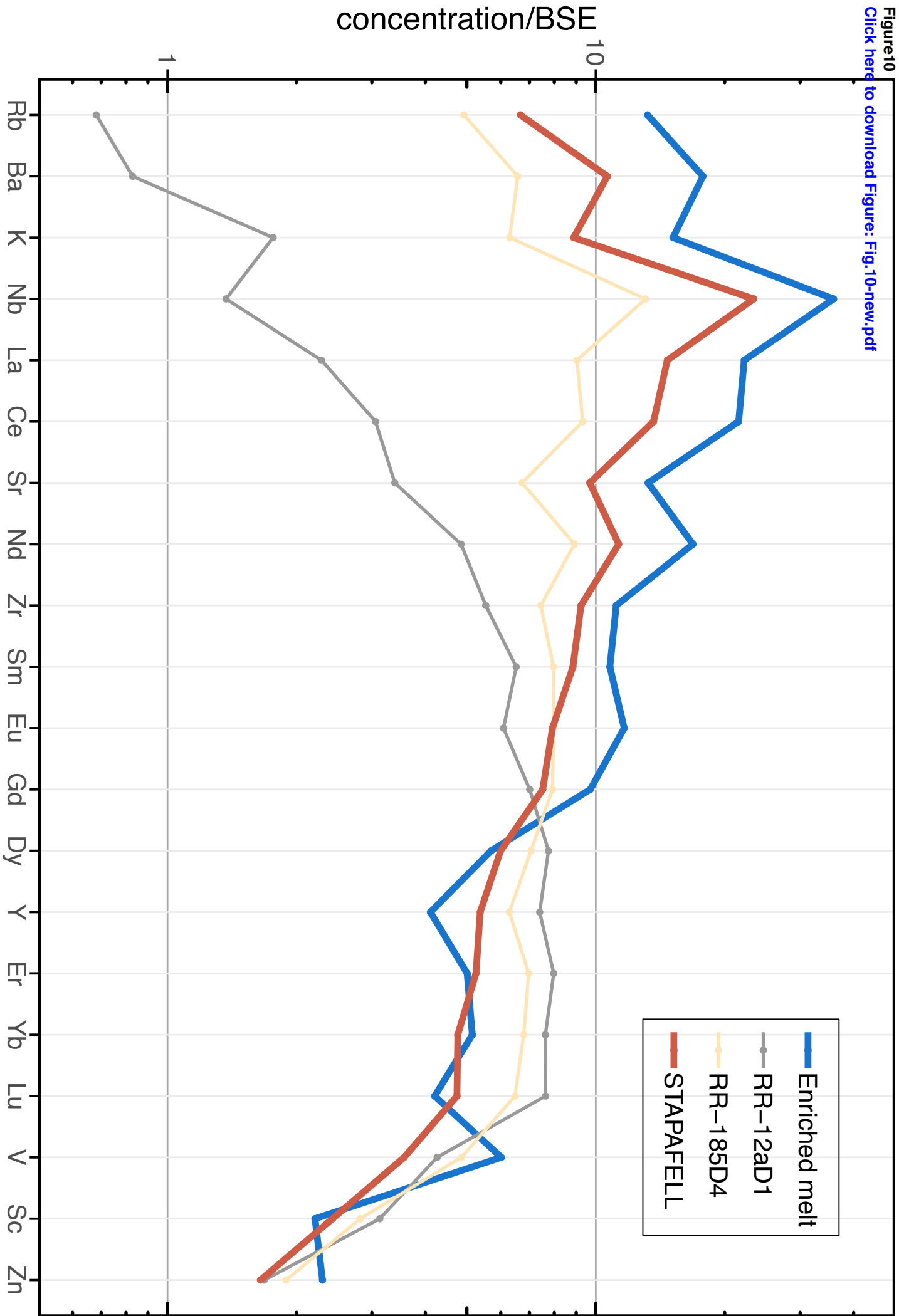**Click here to download Figure: Fig.8-new.pdf**

(a)

(b)

(c)

Figure9|2.5

Figure10
Click here to download Figure: Fig.10-new.pdf
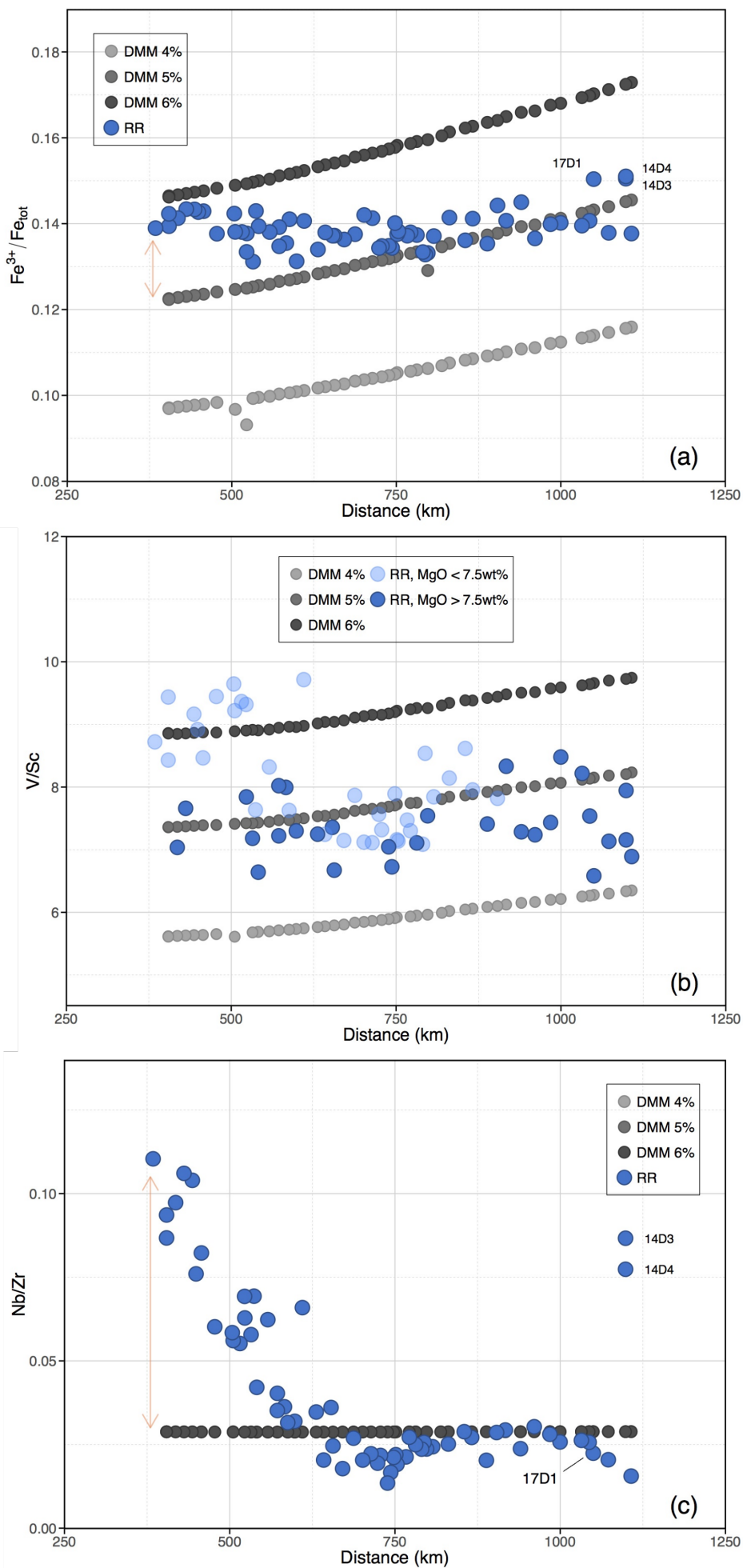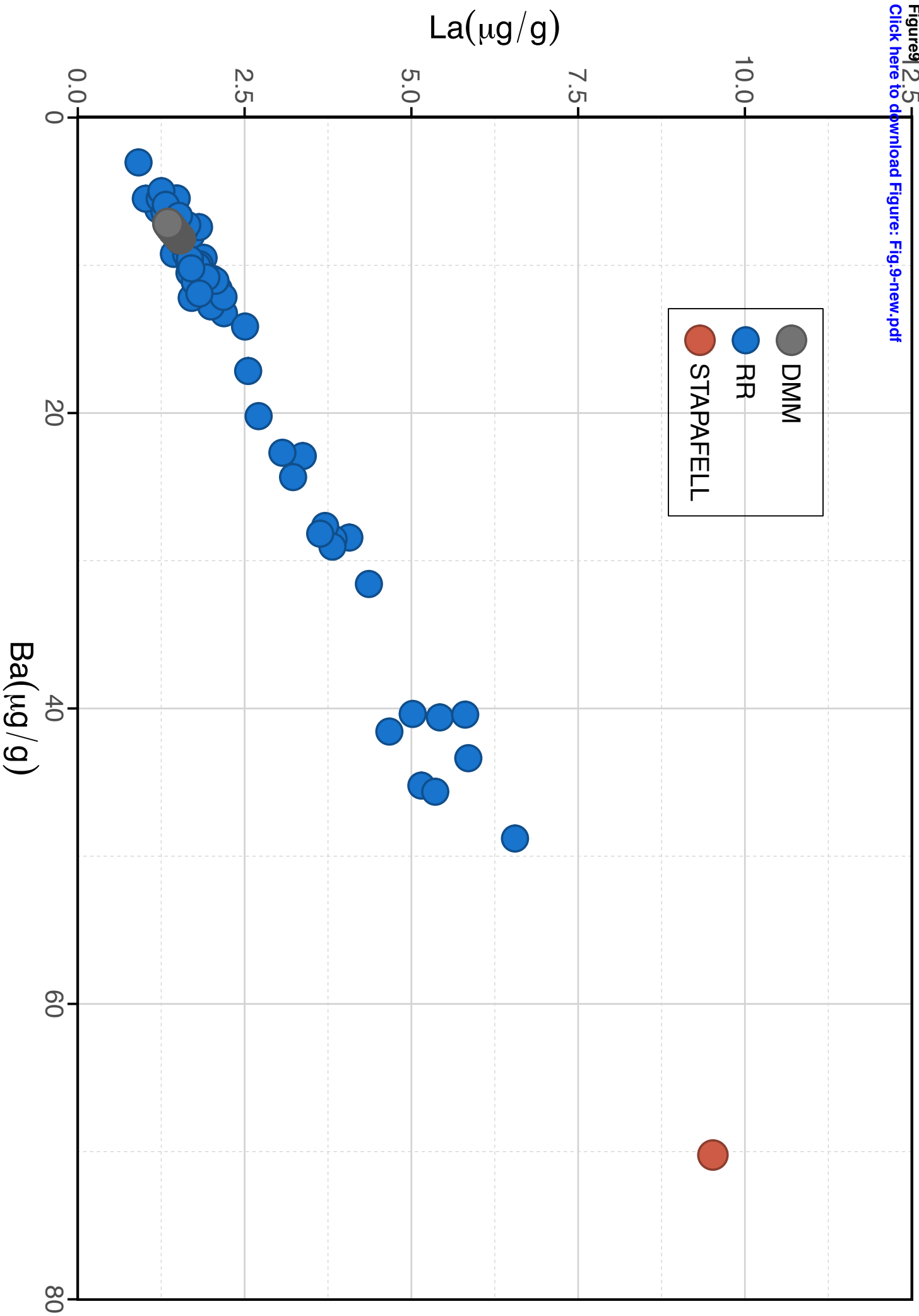
Supplementary Figure S1
Click here to download Supplementary material for online publication only: Fig.S1-new.pdf

Supplementary Figure S2
Click here to download Supplementary material for online publication only: Fig.S2-new.pdf

Supplementary Table 1
Click here to download Supplementary material for online publication only: RR-Supplementary-table-1.pdf

Supplementary Table 2

Supplementary Table 3

Supplementary Table 4

Click here to download Supplementary material for online publication only: RR-Supplementary-table-4-new.pdf

Supplementary Table 5
Click here to download Supplementary material for online publication only: RR-Supplementary-table-5-new.pdf